Finite element hybrid and direct computational aeroacoustics at low Mach numbers in slow time-dependent domains

Oriol Guasch[a], Arnau Pont[a], Joan Baiges[b], Ramon Codina[b]

[a]GTM - Grup de recerca en Tecnologies Mèdia, La Salle, Universitat Ramon Llull
C/ Quatre Camins 2, 08022 Barcelona, Catalonia
[b]Universitat Politècnica de Catalunya,
Jordi Girona 1-3, Edifici C1, 08034 Barcelona, Catalonia

Abstract

In this work, we address the finite element computation of flow noise in the presence of arbitrarily slowly moving rigid bodies at low Mach numbers, by means of hybrid and direct computational aeroacoustics (CAA) strategies. As regards the former, the problem could be dealt with by means of the Ffowcs Williams-Hawkings acoustic analogy. That reduces to Curle's analogy for a static body, which is analogous to a problem of diffraction of sound waves generated by flow eddies in the vicinity of the body. Acoustic analogies in CAA first demand computing the flow motion to extract an acoustic source term from it and then use the latter to calculate the acoustic pressure field. However, in the case of low Mach number flows, the Ffowcs Williams-Hawkings and Curle analogies present a problem as they require knowing the total pressure distribution on the body's boundary (i.e. the aerodynamic pressure plus the acoustic one). As incompressible computational fluid dynamics (CFD) simulations are usually performed to determine the flow motion, the acoustic pressure distribution on the body surface is unavoidably missing, which can yield acoustic analogies inaccurate. In a recent work, it was proposed to tackle that problem for static and rigid surfaces, by keeping the incompressible CFD and then splitting the acoustic pressure into direct and diffracted components. Two separate wave equations were solved for them, in the framework of the finite element method (FEM). In this article, we extend that work to compute the aerodynamic sound generated by a flow interacting with a slowly moving rigid body. The incompressible Navier-Stokes equations are first solved in an arbitrary Lagrangian-Eulerian (ALE) frame of reference to obtain the acoustic source term. Advantage is then taken from the same computational run to separately solve two acoustic ALE wave equations in mixed form for the incident and diffracted acoustic pressure components. For validation of the total acoustic pressure field, an ALE formulation of a direct CAA approach consisting of a unified solver for a compressible isentropic flow in primitive variables is considered. The performance of the exposed methods is illustrated for the aeroacoustics of flow past a slowly oscillating two-dimensional NACA airfoil and for flow exiting a duct with a moving teeth-shaped obstacle at its termination.

Keywords: Computational aeroacoustics, ALE, Flow noise, quadrupolar noise, dipolar noise, diffraction

1. Introduction

The goal of this paper is to extend some of the authors previous finite element methods for computational aeroacoustics (CAA) at low Mach numbers to the case of slow time-dependent domains. Typical related problems could range from aspects concerning the computational generation of sibilant sounds (see e.g., [1–4]) to duct and valve problems in underwater vehicles [5]. In particular, we would like to adapt the hybrid CAA approach for the computation of direct and diffracted aeroacoustic waves in [6] and the direct noise computation (DNC) method consisting of an isentropic compressible solver in [7], to aeroacoustic problems

involving slow moving bodies. Prior to getting into details, however, let us contextualize these two methods in the field of CAA.

Approaches to CAA can be classified into two big groups, namely hybrid CAA and DNC, which are further subdivided into subgroups. The main characteristic of hybrid CAA is that the computation gets split into two parts: a first computational fluid dynamics (CFD) simulation that provides acoustic source terms extracted from the flow motion, and a second simulation which yields the acoustic pressure field (and, in occasions, the acoustic particle velocity as well). As opposed, in DNC a single CFD simulation of a compressible flow is carried out, from which the flow dynamics and the acoustic perturbations naturally arise. The way in which flow and acoustic quantities are separated apart defines the different approaches to hybrid CAA. The most celebrated one is that of acoustic analogies, which started with the pioneering work of Lighthill [8]. The key idea of acoustic analogies is that of reorganizing the compressible Navier-Stokes equations as an inhomogeneous equation involving a wave operator and a source term depending on flow variables [9]. Whether terms in Lighthill's source tensor shall be transferred or not to the acoustic wave operator, as being part of the propagation phenomenon rather than to the source itself, and how to approximate the latter, determines different types of analogies. Some well-known analogies are those of Ribner [10, 11], Phillips [12], Lilley [13], Powell and Howe [14, 15], Möhring [16] and more recently, Goldstein [17]. Another important aspect of acoustic analogies is how to modify them to include the presence of bodies into the flow domain. Curle find an ingenious way to do so by representing the influence of a rigid body as an additional source term consisting of a distribution of dipoles [18]. His method allows one to use the free-space Green function for the wave equation to compute the acoustic pressure field, instead of having to find a tailored Green function satisfying specific boundary conditions at the body's surface. Curle's formulation was generalized to the case of arbitrarily moving bodies by Ffowcs Williams and Hawkings [19].

Acoustic analogies are not the only way to separate flow and acoustic variables and two other common approaches are used in hybrid CAA. If one departs from the continuity, momentum and energy conservation equations for an inviscid fluid and then linearizes them by splitting the flow variables into temporal mean components and acoustic fluctuating ones, the so-called linearized Euler equations (LEE) are obtained [20]. The LEE have been applied to a wide range of problems such as jet [21, 22] and cavity noise [23], among others, and in fact they do not only account for acoustic perturbations but also for vortical end entropy ones. In addition to acoustic analogies and the LEE, the third big subgroup of hybrid CAA methods is that relying on the acoustic perturbation equations (APE) [24], which filter the source terms of the LEE once transformed in the wavenumber-frequency domain. Several formulations of the APE have been proposed, an appealing one for incompressible CFD being the APE-2 (see [24]), recently reformulated in [25] (see also [26] for a stabilized FEM implementation). A complete review on hybrid CAA strategies has been recently published in [27].

In this work we are concerned with acoustic analogies to determine flow noise in the presence of bodies. The first step is to compute the flow motion by means of CFD. In the case of low Mach number flows, the incompressible Navier-Stokes equations are typically solved and then a boundary element method (BEM) is employed to get the acoustic pressure from the analogy integral formulation. Both, Curle's and Ffowcs Williams-Hawkings analogies present a problem though: the strength of the dipole distribution on the static or moving body surface depends on the total pressure, i.e., the aerodynamic plus the acoustic one, but only the former can be obtained from incompressible CFD. To solve that issue, some improvements have been proposed in literature like resorting to the Laplacian Green's function instead of the wave equation one in the integral solution of the analogies [28]. However, one can directly skip the problem by solving both, the CFD and the acoustic wave equation with FEM, avoiding the need of BEM. That is a totally valid approach if one does not need to know the acoustic pressure at very far distances from the source flow region. It only requires making use of the low Mach number approximation for Lighthill's acoustic analogy source term and avoids the inconsistency that appears when solving the integral formulation of Curle's and Ffowcs Williams-Hawkings analogies. This was the option chosen, e.g., in [29–32], but the price to be paid is that it is no longer possible to distinguish the separate acoustic contributions from the body and the flow motion to the total acoustic pressure. To achieve that in the case of a rigid, static body, one can take advantage of the fact that Curle's analogy can be posed as a problem of diffraction [33–35] and solve two, instead of one, acoustic wave equations in the second step of hybrid CAA (one for the direct acoustic field

and the other one for the diffracted field). This was the proposal in [6]. The first, and main, contribution of this work is to revisit the strategy in [6] and extend it to the case of flow noise generation in the presence of slow moving bodies. It will be shown that for a rigid body and small velocities, the Ffowcs Williams-Hawkings analogy can also be viewed as a quasi-stationary diffraction problem. The force exerted by the flow on the body dominates over the rate of change of flow momentum due to the body displacement and it makes sense to establish a separation between incident and diffracted acoustic waves to determine their distinct contributions to the total acoustic pressure. Yet, implementing the hybrid CAA in [6] in moving domains is not straightforward. First, both the incompressible Navier-Stokes and acoustic wave equations need to be solved in an arbitrary Lagrangian-Eulerian frame of reference to account for the computational mesh movement. The quasi-Eulerian approach in [36, 37] will be used for that purpose. Second, it must be taken into account that it is not possible to set the irreducible wave equation in an ALE framework [38], so one must deal with its mixed formulation (namely the linearized continuity and momentum conservation equations for the acoustic pressure and particle velocity [38, 39]). In this work, all these considerations will be accounted for in the splitting strategy of [6]. Emphasis will be put on the acoustic computation, rather than on the incompressible CFD one, for which a vast amount of literature exists in the framework of stabilized FEM.

The second contribution of this work concerns DNC, and in particular the unified isentropic compressible solver in [7], for which a fractional step formulation has been recently derived [40]. DNC presents some advantages and disadvantages when compared to hybrid CAA. On the one hand, it only requires a single CFD simulation for solving the compressible Navier-Stokes equations, yet that turns to be computationally costly unless some simplifications are introduced. DNC directly provides the flow motion, including the acoustic waves, but it does not allow one to distinguish between sound and pseudo-sound in the flow region [41]. On the computational side, DNC has to deal with two main difficulties, namely the performance at low Mach numbers when the flow behaviour is nearly incompressible [42] and the imposition of boundary conditions being valid for both, the flow motion and the acoustic waves [43, 44]. Although several strategies have been proposed to accommodate all compressibility regimes [45–47], those are generally not capable of capturing the aeroacoustic waves as well. A suitable option is to set the equations in primitive variables [48] so they simplify to the incompressible Navier-Stokes equations in the limit of constant density [49]. One can go one step further and assume the flow is isentropic to get rid of the temperature equation and arrive at the compressible approach proposed in [7, 40]. In order to extend the latter for the slow-time dependent domains in this work, we simply need to express the corresponding equations in an ALE framework. Therefore, the basic difference between the herein formulation and that in [7] is that all convective terms in the compressible velocity and pressure equations, and in the boundary conditions, will be now affected by the mesh motion. Given that the hybrid CAA has to deal with an incompressible CFD plus the wave equation in mixed form, the isentropic compressible formulation can become a computationally effective alternative for some aeroacoustic problems (although no distinction between incident and diffracted fields is gathered). As regards the imposition of the boundary conditions, we keep the strategy in [7] where the compressible velocity and pressure were filtered into mean and perturbation (acoustic) fields and different conditions were prescribed for them. Penalization using Nitsche's method [50] was employed to impose Dirichlet conditions in weak form. That option was proved valid in [7] and can be supplemented with a perfectly matched layer (PML) if necessary [51, 52].

All the equations in this work are solved by means of stabilized finite element methods to deal with convective instabilities (either associated to flow convection and/or to the mesh motion) and to use equal interpolation fields for all the involved unknowns. The implemented stabilized FEM belong to the family of variational multi-scale (VMS) methods proposed by Hughes [53, 54]. Although in general we favour the use of orthogonal subgrid scale (OSS) stabilization [55] including time-dependent subscales [56], some simplified models will be introduced for the ease of exposition. An important aspect of some models of VMS FEM stabilization is that for flow dynamics, they have proved capable of implicitly reproducing the large eddy simulation of turbulent flows, without need of pre-filtering the Navier-Stokes equations at the continuous level [56–58]. This is certainly an advantage when dealing with sound generated by turbulent flow motion. A preliminary version of some of the results reported in this work was presented in [59].

The remaining of this paper paper is organized as follows. In section 2, we introduce the generic aeroa-

coustic problem we want to solve and show how for slow-moving bodies it makes sense to identify the Ffowcs Williams-Hawkings analogy with a quasi stationary problem of diffraction. In section 3, we extend the hybrid CAA formulation in [6] by setting the equation in an ALE framework and using the wave equation in mixed form to compute the incident and diffracted acoustic pressure and velocity fields. The ALE formulation of the isentropic compressible flow solver in [7] is presented in section 4. Section 5 introduces two numerical examples to illustrate the performance of the methods exposed in the previous sections. The case of a slowly oscillating two-dimensional NACA0012 airfoil with its center of rotation placed the leading edge is studied, as well as the case of a duct termination with a moving teeth-shaped object at its end. Conclusions close the paper in section 6.

2. Flow noise for slow moving rigid bodies as a diffraction problem

2.1. Ffowcs Williams-Hawkings analogy and related diffraction problem

The Ffowcs Williams-Hawkings (FWH) analogy provides a formal solution to the problem of flow noise generation in the presence of arbitrary moving surfaces. In addition to Lighthill's quadrupolar source term for aerodynamic noise production in free space [8], the influence of moving boundaries is included in the FWH formulation by means of additional dipole and monopole source terms in the inhomogeneous wave equation for the acoustic pressure. This allows one to solve the latter using the free-space Green function. The acoustic density fluctuations in a domain $\Omega_{\mathrm{ac}}(t) \subset \mathbb{R}^d$ $(d = 2, 3)$ resulting from flow motion and its interaction with a moving body of volume $\Omega_b(t)$ and boundary $\Gamma_b(t)$ (see Fig. 1, which is to be compared with Fig. 1 in [6]) is provided by [19, 60],

$$
\begin{aligned}
H(f)c_0^2 \left(\rho - \rho_0 \right)(\boldsymbol{x}, t) = {} & \frac{\partial^2}{\partial x_i \partial x_j} \int_{\Omega_{\mathrm{ac}}(\tau)} [T_{ij}] \frac{\mathrm{d}^3 \boldsymbol{y}}{4\pi \mid \boldsymbol{x} - \boldsymbol{y} \mid} \\
& - \frac{\partial}{\partial x_i} \int_{\Gamma_b(\tau)} \left[\rho v_i \left(v_i - v_j^b \right) + p_{ij}' \right] \frac{dS_j(\boldsymbol{y})}{4\pi \mid \boldsymbol{x} - \boldsymbol{y} \mid} \\
& + \frac{\partial}{\partial t} \int_{\Gamma_b(\tau)} \left[\rho v_i \left(v_i - v_j^b \right) + \rho_0 v_j^b \right] \frac{dS_j(\boldsymbol{y})}{4\pi \mid \boldsymbol{x} - \boldsymbol{y} \mid},
\end{aligned}
\tag{1}
$$

where ρ stands for the total density, ρ_0 for the average one and c_0 for the speed of sound. T_{ij} in the first line of (1) represents Lighthill's tensor while, in the second line $p_{ij}' \equiv P\delta_{ij} - \sigma_{ij}$ with P being the full compressible flow pressure. σ_{ij} denotes the viscous stress tensor. In the second and third lines, v_i designates the i-th component of the flow velocity vector $\boldsymbol{v}$ and v_i^b the i-th component of the body velocity $\boldsymbol{v}^b$. The square brackets in the integrals denote, as usual, evaluation at the retarded time $\tau := t - |\boldsymbol{x} - \boldsymbol{y}|/c_0$. The surface differential in the boundary integrals is given by $dS_j = n_j dS$, with n_j being the j-th component of the normal vector pointing outwards the surface S. H is the Heaviside function so that $H(f) = 1$ in $\Omega_{ac}(t)$ and $H(f) = 0$ in $\Omega_b(t)$ (i.e., f is defined such that $f > 0$ in Ω_{ac} and $f < 0$ in Ω_b). The term in the first line involves a spatial double divergence and therefore stands for a quadrupole source contribution, while the term in the second line acts as a dipole distribution. That in the third line represents a monopole. In the case of a stationary rigid body surface, the FWH analogy in (1) reduces to Curle's analogy [18, 60].

In this work, we will be concerned with the following simplifications in (1). First, low Mach number (M) flows will be assumed for which Lighthill's tensor can be approximated by the Reynolds stress, i.e., $T_{ij} \approx \rho_0 u_i^0 u_j^0$, with u_i^0 standing for the i-th component of the incompressible flow velocity $\boldsymbol{u}^0$. In addition, high Reynolds numbers will be considered so that $\sigma_{ij} \approx 0$. Moreover, only the case of rigid bodies will be
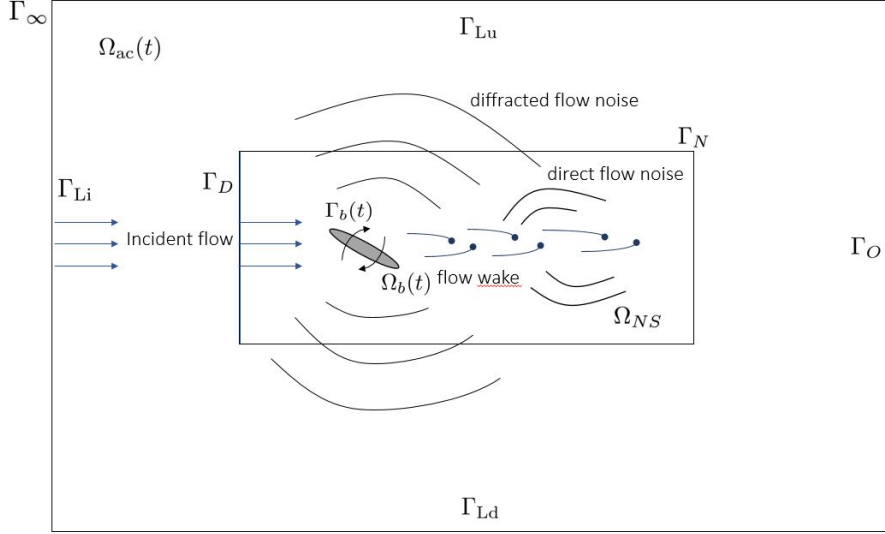
4

Figure 1: Sketch for the aeroacoustic problem. Noise generated by flow past a slowly moving body. Direct (incident) and diffracted acoustic pressure components. The Navier-Stokes computational domain Ω_{NS} only makes sense for the first step of the hybrid CAA approach of section 3. The isentropic compressible flow simulation in section 4 is totally performed in $\Omega_{\mathrm{ac}}(t)$. The body is rigid so the volume of the acoustic and body domains are constant but can change their shape.

addressed for which $\boldsymbol{v} = \boldsymbol{v}^b$ at Γ_b. Inserting these assumptions in (1) yields,

$$H(f)c_0^2\left(\rho - \rho_0\right)(\boldsymbol{x}, t) = \frac{\partial^2}{\partial x_i \partial x_j} \int_{\Omega_{\mathrm{ac}}(\tau)} \left[\rho_0 u_i^0 u_j^0\right] \frac{\mathrm{d}^3\boldsymbol{y}}{4\pi \mid \boldsymbol{x} - \boldsymbol{y} \mid}$$
$$- \frac{\partial}{\partial x_i} \int_{\Gamma_b(\tau)} \left[P\delta_{ij}\right] \frac{dS_j\left(\boldsymbol{y}\right)}{4\pi \mid \boldsymbol{x} - \boldsymbol{y} \mid}$$
$$+ \frac{\partial}{\partial t} \int_{\Gamma_b(\tau)} \left[\rho_0 v_j^b\right] \frac{dS_j\left(\boldsymbol{y}\right)}{4\pi \mid \boldsymbol{x} - \boldsymbol{y} \mid}. \tag{2}$$

As explained above, the third term in the right hand side (r.h.s) corresponds to a monopole distribution. However, one could not expect a net outflow of volume flow from a rigid surface so the monople integral must correspond to a combination of higher order multipoles. This is a well-known fact and it is shown e.g., in [41, 60] how this term corresponds to the summation of a dipole distribution plus a quadrupole one, which involve integrals over the interior of the body Ω_b of expressions depending on the body velocity $\boldsymbol{v}^b$. We do not reproduce this result here though, as it is unnecessary for the forthcoming discussion.

The most typical application of (2) concerns propeller and rotor noise. In such case, the dipole and "monopole" terms in (2) clearly dominate noise production at the far field and the quadrupole one can be neglected. The noise generated by the dipole distribution is usually referred to as the loading noise, while that of the "monopole" is known as the thickness noise. When the magnitude of the body velocity $|\boldsymbol{v}_b|$ is high (e.g., a helicopter, turbine or fan blade), both the loading and thickness noise significantly contribute to the overall acoustic pressure. However, if the body moves very slowly, the monopole contribution will be small as compared to the dipole one. In fact, it can be proved that for compact bodies (i.e. when $\ell \equiv \mathrm{diam}(\Omega_b) \ll \lambda$, λ being the acoustic wavelength) variations in retarded time are negligible and at the far field, where as said the quadrupole terms become insignificant, we get (see [41]),

$$c_0^2\left(\rho - \rho_0\right)(\boldsymbol{x}, t) \approx p(\boldsymbol{x}, t) \underset{\boldsymbol{x} \to \infty}{\sim} -\frac{1}{4\pi} \frac{\partial}{\partial x_i} \left[\frac{f_i + \rho_0 \ell^3 D v_i / Dt}{\left|1 - \frac{x_i v_i}{|\boldsymbol{x}|c_0}\right|}\right] \sim -\frac{1}{4\pi} \frac{\partial}{\partial x_i} \left[f_i + \rho_0 \ell^3 D v_i / Dt\right]. \tag{3}$$

5

In this equation, f_i represents the total force exerted by the flow on the body surface Γ_b in the i-th direction and $\rho_0 \ell^3 Dv_i/Dt$ would be the rate of change of momentum of the body if it had density ρ_0, also in the i-th direction. In the second approximation we have neglected the Doppler factor in the denominator as M $\ll$ 1. Equation (3) represents a dipole acoustic source whose strength is slightly modified by the body motion. As mentioned in the Introduction, such circumstance can be encountered, for instance, in sibilant and syllable voice production or in the slow closing of a duct termination conveying a flow. The motion of the body (e.g., the teeth in the mouth) will essentially alter the flow eddy pattern and diffract the acoustic waves they generate, but will not act as a direct and substantial source of sound (i.e., $\rho_0 \ell^3 Dv_i/Dt$ would be negligible in front of f_i if the body moves very slowly). Essentially, the problem will be very similar to that encountered when considering flow noise generation by a rigid and stationary surface. As said above, such case is described by Curle's analogy and it is well-known that such analogy can also be viewed as a diffraction problem for the acoustic waves generated by quadrupole sources due to flow motion close to a rigid, stationary body [33–35]. We could therefore refer to the situation we want to handle in this paper as that of a quasi-stationary diffraction problem.

Let us assume, that a tailored Green function $G(\boldsymbol{x}, t \mid \boldsymbol{y}, \tau)$ was available for the noise problem in Fig. 1, satisfying appropriate boundary conditions on $\Gamma_b(t)$. That would directly provide the acoustic pressure field generated by the flow motion interacting with the moving surface as,

$$p(\boldsymbol{x}, t) = \int_{-\infty}^{\infty} \int_{\Omega_{ac}(\tau)} G(\boldsymbol{x}, t \mid \boldsymbol{y}, \tau) \frac{\partial^2}{\partial y_i \partial y_j}(\rho_0 u_i^0 u_j^0) d^3\boldsymbol{y} d\tau, \tag{4}$$

where, as seen in (3), $p(\boldsymbol{x}, t) = c_0^2 (\rho - \rho_0)(\boldsymbol{x}, t)$. If the body was translating, rotating and/or oscillating very slowly so that its movement was unable to generate sound waves, we could set the problem in Fig. 1 as a quasi-stationary diffraction problem and split the Green function in (4) as the free-space one (i.e,. in the absence of the body) plus the body diffraction contribution, namely

$$G(\boldsymbol{x}, t \mid \boldsymbol{y}, \tau) = G_F(\boldsymbol{x}, t \mid \boldsymbol{y}, \tau) + G_D(\boldsymbol{x}, t \mid \boldsymbol{y}, \tau), \tag{5}$$

with

$$G_F(\boldsymbol{x}, t \mid \boldsymbol{y}, \tau) = \frac{1}{4\pi|\boldsymbol{x} - \boldsymbol{y}|}\delta\left(t - \tau - \frac{|\boldsymbol{x} - \boldsymbol{y}|}{c_0}\right), \tag{6}$$

δ being the Dirac delta function. Inserting (5) into (4), integrating by parts and considering (6), provides

$$p(\boldsymbol{x}, t) = \frac{\partial^2}{\partial x_i \partial x_j} \int_{\Omega_{ac}(\tau)} \frac{1}{4\pi|\boldsymbol{x} - \boldsymbol{y}|}\left[\rho_0 u_i^0 u_j^0\right] d^3\boldsymbol{y} + \int_{-\infty}^{\infty} \int_{\Omega_{ac}(\tau)} G_D \frac{\partial^2}{\partial y_i \partial y_j}(\rho_0 u_i^0 u_j^0) d^3\boldsymbol{y} d\tau. \tag{7}$$

Comparing (7) with (2) allows one to mathematically identify the diffracted acoustic pressure contribution in (7) with the dipole and monopole distributions in (2),

$$\int_{-\infty}^{\infty} \int_{\Omega_{ac}(\tau)} G_D \frac{\partial^2}{\partial y_i \partial y_j}(\rho_0 u_i^0 u_j^0) d^3\boldsymbol{y} d\tau = -\frac{\partial}{\partial x_i} \int_{\Gamma_b(\tau)} \left[P\delta_{ij}\right] \frac{dS_j(\boldsymbol{y})}{4\pi \mid \boldsymbol{x} - \boldsymbol{y} \mid}$$
$$+ \frac{\partial}{\partial t} \int_{\Gamma_b(\tau)} \left[\rho_0 v_j^b\right] \frac{dS_j(\boldsymbol{y})}{4\pi \mid \boldsymbol{x} - \boldsymbol{y} \mid}. \tag{8}$$

For the identification to make full physical sense in the context of diffraction, the monopole term should be small as discussed for equation (3), so that

$$\int_{-\infty}^{\infty} \int_{\Omega_{ac}(\tau)} G_D \frac{\partial^2}{\partial y_i \partial y_j}(\rho_0 u_i^0 u_j^0) d^3\boldsymbol{y} d\tau \approx -\frac{\partial}{\partial x_i} \int_{\Gamma_b(\tau)} \left[P\delta_{ij}\right] \frac{dS_j(\boldsymbol{y})}{4\pi \mid \boldsymbol{x} - \boldsymbol{y} \mid}. \tag{9}$$

In what follows, it will be assumed that (9) is essentially valid.

6

It shall be noted that if we remove the monopole component from the simplified FWH in (2) we basically recover Curle's analogy except for the fact that now the body can have some slow motion. One could therefore compute the generated flow noise by solving the corresponding integrals in the time varying domains. Unfortunately, such procedure inherits the same flaw as Curle's analogy if one derives the terms in the integrals from an incompressible CFD simulation. While the latter provides the incompressible flow velocity and pressure fields, $\boldsymbol{u}^0$ and p^0, the total pressure (i.e., including the acoustic fluctuations) is needed in the integrand of the dipole term. A way out to this problem is to exploit the relation we have established between the FWH analogy in (2) and the diffraction problem in (9), and abandon the framework of the FWH integral formulation. Our proposal is to resort to a hybrid CAA approach consisting of a first incompressible CFD simulation to obtain $\boldsymbol{u}^0$ and p^0 and, in the same computational run, solve two separate wave equations, one for the incident acoustic pressure and the other one for the diffracted pressure. This idea was proposed in [6] for the case of a rigid and stationary body and will be extended in next section to slowly moving surfaces. All involved equations are solved by means of subgrid scale stabilized FEM to be detailed in section 3.

2.2. Flow noise problem in an arbitrary Lagrangian-Eulerian frame of reference

Before presenting how to apply the flow noise formulation in [6] to the case of slow moving domains, let us introduce some considerations for the problem at hand. The first thing we should realize is that all involved partial differential equations (PDE), namely the incompressible Navier-Stokes equation to describe the flow dynamics and the acoustic wave equation for the aerodynamic generated sound must be set in arbitrary Lagrangian-Eulerian (ALE) framework to account for the domain time variation. An efficient way to do so is by means of a quasi-Eulerian approach [36, 37] in which the time derivative of any variable is expressed in a referential frame that moves with the domain, while the variable spatial partial derivatives are kept in an Eulerian framework. If g denotes a generic variable and $\boldsymbol{u}_{\mathrm{dom}}$ stands for the domain velocity, which in a numerical simulation is identified with the mesh velocity at every node, one should replace $\partial_t g$ in the corresponding PDE by $\partial_t g - \boldsymbol{u}_{\mathrm{dom}} \cdot \nabla g$.

The second point is to recognize that it is not possible to find an irreducible wave equation for the acoustic pressure in an ALE framework and one must deal, instead, with the linearized continuity and momentum equations to describe acoustic wave propagation [38]. These are given by,

$$\frac{1}{\rho_0 c_0^2} \frac{\partial p}{\partial t} + \nabla \cdot \boldsymbol{u} = Q, \tag{10a}$$

$$\rho_0 \frac{\partial \boldsymbol{u}}{\partial t} + \nabla p = \boldsymbol{f}, \tag{10b}$$

and are sometimes shortly referred to as the wave equation in mixed form [39]. Here, $p(\boldsymbol{x}, t)$ designates the acoustic pressure and $\boldsymbol{u}(\boldsymbol{x}, t)$ the acoustic particle velocity. The inhomogeneous terms $Q(\boldsymbol{x}, t)$ and $\boldsymbol{f}(\boldsymbol{x}, t)$ respectively represent a volume source distribution and an external body force per unit volume.

Expressing (10) in an ALE frame of reference results in

$$\frac{1}{\rho_0 c_0^2} \frac{\partial p}{\partial t} - \frac{1}{\rho_0 c_0^2} \boldsymbol{u}_{\mathrm{dom}} \cdot \nabla p + \nabla \cdot \boldsymbol{u} = Q, \tag{11a}$$

$$\rho_0 \frac{\partial \boldsymbol{u}}{\partial t} - \rho_0 \boldsymbol{u}_{\mathrm{dom}} \cdot \nabla \boldsymbol{u} + \nabla p = \boldsymbol{f}. \tag{11b}$$

To solve the flow noise problem in Fig. 1, equation (11) must be supplemented with appropriate initial and boundary conditions. These are given by,

$$\boldsymbol{u} \cdot \boldsymbol{n} = \boldsymbol{u}_{\mathrm{dom}} \cdot \boldsymbol{n} \quad \text{on } \Gamma_{\mathrm{b}}(t) \ t > 0, \tag{12a}$$

$$\boldsymbol{u} \cdot \boldsymbol{n} = \frac{1}{Z_0} p \quad \text{on } \Gamma_\infty \ t > 0, \tag{12b}$$

$$p(\boldsymbol{x}, 0) = 0, \ \boldsymbol{u}(\boldsymbol{x}, 0) = \boldsymbol{0}, \quad \text{in } \Omega_{\mathrm{ac}}(t), \ t = 0, \tag{12c}$$

where (12b) is nothing but Sommerfeld's radiation condition in mixed form (see e.g., [61]) and $Z_0 = \rho_0 c_0$ is the fluid acoustic impedance. In what concerns the source terms Q and $\boldsymbol{f}$ in (11), they will depend on the acoustic analogy under consideration. For instance, in Ribner's one [10, 11] the inhomogeneous source term for the irreducible wave equation is $c_0^2 \partial^2 p^0 / \partial t^2$, while for Lighthill's low Mach number approximation the source becomes $\rho_0 \partial^2 (u_i^0 u_j^0) / \partial x_i \partial x_j$. If one deals with the wave equation in mixed form in an ALE framework in (11), these source terms can be formulated as,

$$\text{Lighthill's analogy}: \ f_i = -\rho_0 \frac{\partial (u_i^0 u_j^0)}{\partial x_j}, \quad Q = 0 \tag{13a}$$

$$\text{Ribner's analogy}: \ \boldsymbol{f} = \boldsymbol{0}, \quad Q = -(1/\rho_0 c_0^2) \left[\frac{\partial p^0}{\partial t} - \boldsymbol{u}_{\text{dom}} \cdot \nabla p^0 \right]. \tag{13b}$$

The incompressible velocity field in (13a) and the incompressible pressure field in (13b) are to be obtained from the solution of the ALE incompressible Navier-Stokes equations, namely (see Fig. 1),

$$\frac{\partial \boldsymbol{u}^0}{\partial t} - \nu \Delta \boldsymbol{u}^0 + \left(\boldsymbol{u}^0 - \boldsymbol{u}_{\text{dom}} \right) \cdot \nabla \boldsymbol{u}^0 + \nabla p^0 = \boldsymbol{f} \quad \text{in } \Omega_{NS}(t), \ t > 0, \tag{14a}$$

$$\nabla \cdot \boldsymbol{u}^0 = 0 \quad \text{in } \Omega_{NS}(t), \ t > 0, \tag{14b}$$

$$\boldsymbol{u}^0 (\boldsymbol{x}, 0) = \boldsymbol{u}_0^0 (\boldsymbol{x}) \quad \text{in } \Omega_{NS}(t), \ t = 0, \tag{14c}$$

$$\boldsymbol{u}^0 (\boldsymbol{x}, t) = \boldsymbol{u}_{\text{dom}} (\boldsymbol{x}, t) \quad \text{on } \Gamma_{\text{b}}(t), \ t > 0, \tag{14d}$$

$$\boldsymbol{u}^0 (\boldsymbol{x}, t) = \boldsymbol{u}_D^0 (\boldsymbol{x}, t) + \boldsymbol{u}_{\text{dom}} (\boldsymbol{x}, t) \quad \text{on } \Gamma_D(t), \ t > 0, \tag{14e}$$

$$\boldsymbol{n} \cdot \boldsymbol{\sigma} (\boldsymbol{x}, t) = \boldsymbol{t}_N (\boldsymbol{x}, t) \quad \text{on } \Gamma_N(t), \ t > 0, \tag{14f}$$

where, $\Omega_{NS}(t)$ corresponds to the computational domain where the Navier-Stokes equations are solved (which does not need to necessarily coincide with $\Omega_{ac}(t)$) and Γ_D and Γ_N respectively denote boundaries with prescribed Dirichlet and Neumann conditions. $\boldsymbol{n}$ is the outward pointing normal at the boundary and $\boldsymbol{t}_N$ stands for the traction.

2.3. Splitting the total acoustic pressure into incident and diffracted components

At this point we have all ingredients to apply the flow noise strategy in [6] to the current problem with time varying domains. The key idea is to split the acoustic fields into incident and diffracted components. As quoted in [6], this is valid for any general linear wave operator. In the current case, the operator is the wave equation in mixed form, which acts both on the acoustic pressure p and on the acoustic particle velocity $\boldsymbol{u}$. If we take $\boldsymbol{u} = \boldsymbol{u}_{\text{i}} + \boldsymbol{u}_{\text{d}}$ and $p = p_{\text{i}} + p_{\text{d}}$ in (11), the subscripts i and d respectively standing for incident and diffracted, we are left with the incident field problem

$$\frac{1}{\rho_0 c_0^2} \partial_t p_{\text{i}} - \frac{1}{\rho_0 c_0^2} \boldsymbol{u}_{\text{dom}} \cdot \nabla p_{\text{i}} + \nabla \cdot \boldsymbol{u}_{\text{i}} = Q \quad \text{in } \Omega_{ac}(t) \cup \Omega_{\text{b}}(t), \ t > 0, \tag{15a}$$

$$\rho_0 \partial_t \boldsymbol{u}_{\text{i}} - \rho_0 \boldsymbol{u}_{\text{dom}} \cdot \nabla \boldsymbol{u}_{\text{i}} + \nabla p_{\text{i}} = \boldsymbol{f} \quad \text{in } \Omega_{ac}(t) \cup \Omega_{\text{b}}(t), \ t > 0, \tag{15b}$$

$$\boldsymbol{u}_{\text{i}} \cdot \boldsymbol{n} = \frac{1}{Z_0} p_{\text{i}} \quad \text{on } \Gamma_\infty, \ t > 0, \tag{15c}$$

$$p_{\text{i}} (\boldsymbol{x}, 0) = 0, \ \boldsymbol{u}_{\text{i}} (\boldsymbol{x}, 0) = \boldsymbol{0}, \quad \text{in } \Omega_{ac}(t) \cup \Omega_{\text{b}}(t), \ t = 0, \tag{15d}$$

and the diffracted one,

$$\frac{1}{\rho_0 c_0^2} \partial_t p_{\text{d}} - \frac{1}{\rho_0 c_0^2} \boldsymbol{u}_{\text{dom}} \cdot \nabla p_{\text{d}} + \nabla \cdot \boldsymbol{u}_{\text{d}} = 0 \quad \text{in } \Omega_{ac}(t), \ t > 0, \tag{16a}$$

$$\rho_0 \partial_t \boldsymbol{u}_{\text{d}} - \rho_0 \boldsymbol{u}_{\text{dom}} \cdot \nabla \boldsymbol{u}_{\text{d}} + \nabla p_{\text{d}} = \boldsymbol{0} \quad \text{in } \Omega_{ac}(t), \ t > 0, \tag{16b}$$

$$\boldsymbol{u}_{\text{d}} \cdot \boldsymbol{n} = (\boldsymbol{u}_{\text{dom}} - \boldsymbol{u}_{\text{i}}) \cdot \boldsymbol{n} \quad \text{on } \Gamma_{\text{b}}(t), \ t > 0, \tag{16c}$$

$$\boldsymbol{u}_{\text{d}} \cdot \boldsymbol{n} = \frac{1}{Z_0} p_{\text{d}} \quad \text{on } \Gamma_\infty, \ t > 0, \tag{16d}$$

$$p_{\text{d}} (\boldsymbol{x}, 0) = 0, \ \boldsymbol{u}_{\text{d}} (\boldsymbol{x}, 0) = \boldsymbol{0}, \quad \text{in } \Omega_{ac}(t), \ t = 0. \tag{16e}$$

Note that the summation of problems (15) and (16) recovers the original one in (11), with the initial and boundary conditions prescribed in (12). Furthermore, one should be aware of a tricky aspect of equations (15) and (16). They are not solved in the same computational domains. To simulate the incident field one has to include the region occupied by the body as part of the computational domain, while this has to be removed when solving the wave equation for the diffracted pressure. That is, the wave equation for p_i is solved in $\Omega_\mathrm{ac}(t) \cup \Omega_\mathrm{b}(t)$ while that for p_d is solved in $\Omega_\mathrm{ac}(t)$ (see equations (15a) and (16a)). The incident acoustic particle velocity enters the diffracted wave equation through the boundary condition (16c).

In what follows, our goal consists in solving the wave equations (15) and (16) together with the incompressible Navier-Stokes equations in (14) to obtain the flow noise source terms, using a finite element approach. The weak formulation and discretization for the latter will be not presented as it can be found elsewhere in literature (see e.g., [55, 56, 58] among many others) and we will concentrate on equations (15) and (16). Later, in section 4, we will introduce the ALE formulation for the isentropic compressible solver in [7], which will be used for comparison purposes. Its FEM and time discretization will be briefly exposed as it has not been published before.

3. Numerical discretization of the acoustic wave equation in mixed form for the incident and diffracted acoustic pressure fields

3.1. Continuous weak form of the incident and diffracted wave problems

To discretize the wave equations in mixed form (15) and (16) using a FEM approach we first need to express them in weak form. To that goal, we proceed as usual by multiplying equations (15a) and (16a) with the scalar test function q, and equations (15b) and (16b) with the vector test function $\boldsymbol{v}$. The resulting scalar equations are then integrated over their respective computational domains $\Omega_\mathrm{ac}(t) \cup \Omega_\mathrm{b}(t)$ and $\Omega_\mathrm{ac}(t)$. If the problems are solved in the time interval $[0, T]$ and we denote by $(f, g) := \int_\Omega f g \, d\Omega$ the integral of the product of functions f and g, the weak formulation of (15) and (16) will read as follows.

For the incident pressure field, we need to find find $p_\mathrm{i} \in \mathcal{W}_p^\mathrm{i}([0, T], \mathcal{V}_p^\mathrm{i})$ and $\boldsymbol{u}_\mathrm{i} \in \boldsymbol{\mathcal{W}}_{\boldsymbol{u}}^\mathrm{i}([0, T], \boldsymbol{\mathcal{V}}_{\boldsymbol{u}}^\mathrm{i})$ such that

$$\frac{1}{\rho_0 c_0^2}(\partial_t p_\mathrm{i}, q) - \frac{1}{\rho_0 c_0^2}(\boldsymbol{u}_\mathrm{dom} \cdot \nabla p_\mathrm{i}, q) + (\nabla \cdot \boldsymbol{u}_\mathrm{i}, q) = (Q, q) \quad \forall \, q \in \mathcal{V}_p^\mathrm{i}, \tag{17a}$$

$$\rho_0(\partial_t \boldsymbol{u}_\mathrm{i}, \boldsymbol{v}) - \rho_0(\boldsymbol{u}_\mathrm{dom} \cdot \nabla \boldsymbol{u}_\mathrm{i}, \boldsymbol{v}) + (\nabla p_\mathrm{i}, \boldsymbol{v}) = (\boldsymbol{f}, \boldsymbol{v}) \quad \forall \, \boldsymbol{v} \in \boldsymbol{\mathcal{V}}_{\boldsymbol{u}}^\mathrm{i}, \tag{17b}$$

where $\mathcal{W}_p^\mathrm{i}$, $\boldsymbol{\mathcal{W}}_{\boldsymbol{u}}^\mathrm{i}$, $\mathcal{V}_p^\mathrm{i}$ and $\boldsymbol{\mathcal{V}}_{\boldsymbol{u}}^\mathrm{i}$ stand for suitable functional spaces for the incident acoustic pressure and acoustic particle velocity that will not be described here to avoid technicalities (see e.g., [38] for details). In what concerns the variational formulation for the diffracted problem, this consists in finding $p_\mathrm{d} \in \mathcal{W}_p^\mathrm{d}([0, T], \mathcal{V}_p^\mathrm{d})$ and $\boldsymbol{u}_\mathrm{d} \in \boldsymbol{\mathcal{W}}_{\boldsymbol{u}}^\mathrm{d}([0, T], \boldsymbol{\mathcal{V}}_{\boldsymbol{u}}^\mathrm{d})$ such that

$$\frac{1}{\rho_0 c_0^2}(\partial_t p_\mathrm{d}, q) - \frac{1}{\rho_0 c_0^2}(\boldsymbol{u}_\mathrm{dom} \cdot \nabla p_\mathrm{d}, q) + (\nabla \cdot \boldsymbol{u}_\mathrm{d}, q) - (q, \boldsymbol{u}_\mathrm{d} \cdot \boldsymbol{n})_{\Gamma_\mathrm{b}} = -(q, (\boldsymbol{u}_\mathrm{dom} - \boldsymbol{u}_\mathrm{i}) \cdot \boldsymbol{n})_{\Gamma_\mathrm{b}} \quad \forall \, q \in \mathcal{V}_p^\mathrm{d}, \tag{18a}$$

$$\rho_0(\partial_t \boldsymbol{u}_\mathrm{d}, \boldsymbol{v}) - \rho_0(\boldsymbol{u}_\mathrm{dom} \cdot \nabla \boldsymbol{u}_\mathrm{d}, \boldsymbol{v}) - (\nabla \cdot \boldsymbol{v}, p_\mathrm{d}) + (\boldsymbol{v} \cdot \boldsymbol{n}, p_\mathrm{d})_{\Gamma_\mathrm{b}} + \alpha(\boldsymbol{v} \cdot \boldsymbol{n}, \boldsymbol{u}_\mathrm{d} \cdot \boldsymbol{n} - (\boldsymbol{u}_\mathrm{dom} - \boldsymbol{u}_\mathrm{i}) \cdot \boldsymbol{n})_{\Gamma_\mathrm{b}} = 0$$
$$\forall \, \boldsymbol{v} \in \boldsymbol{\mathcal{V}}_{\boldsymbol{u}}^\mathrm{d}. \tag{18b}$$

Here, $(\cdot, \cdot)_{\Gamma_\mathrm{b}}$ denotes the integral on the boundary Γ_b, and, once again, $\mathcal{W}_p^\mathrm{d}$, $\boldsymbol{\mathcal{W}}_{\boldsymbol{u}}^\mathrm{d}$, $\mathcal{V}_p^\mathrm{d}$ and $\boldsymbol{\mathcal{V}}_{\boldsymbol{u}}^\mathrm{d}$ designate appropriate functional spaces for the diffracted acoustic pressure and acoustic particle velocity, which will be not specified. Note that the Dirichlet boundary conditions (15c), (16c) and (16d) must be prescribed strongly on $\Gamma_\mathrm{b}(t)$ and Γ_∞ for problems (17) and (18). However, since the code reads a full mesh where Γ_b belongs to interior nodes, it would be convenient to set the strong condition $\boldsymbol{u}_\mathrm{d} \cdot \boldsymbol{n} = (\boldsymbol{u}_\mathrm{dom} - \boldsymbol{u}_\mathrm{i}) \cdot \boldsymbol{n}$ in weak form. To that goal we have symmetrized (18) to employ Nitsche's method [50] using a penalty parameter $\alpha = \beta \frac{\rho_0 |\boldsymbol{u}_d|}{h}$. For the present case, $\beta = 1$ has sufficed to enforce the boundary condition on Γ_b.

3.2. Spatial discretization: stabilized finite element method

The FEM discretization of the wave equations in mixed form (17) and (18) is not straightforward. Even in the case of no convection, instabilities occur if equal order interpolation is employed for the pressure and velocity fields [39]. To avoid using different interpolations for p and $\boldsymbol{u}$, one can resort to FEM stabilized approaches like those based in the VMS method, see e.g. [53, 54]. In this work, we will follow the VMS strategy in [38, 62] to deal with waves set in an ALE framework and/or in the presence of convection. Orthogonal subgrid scales (OSS), (see [39, 55]), will be employed to eliminate the instabilities encountered when directly applying the Galerkin FEM to (17) and (18).

Let us introduce the FEM spaces $\mathcal{V}_{p_h}^{\mathrm{i}} \subset \mathcal{V}_p^{\mathrm{i}}$ and $\boldsymbol{\mathcal{V}}_{\boldsymbol{u}_h}^{\mathrm{i}} \subset \boldsymbol{\mathcal{V}}_{\boldsymbol{u}}^{\mathrm{i}}$. The discrete stabilized FEM formulation of the incident problem (17) becomes that of finding $p_{\mathrm{i}_h} \in \mathcal{W}_p^{\mathrm{i}}([0,T], \mathcal{V}_{p_h}^{\mathrm{i}})$ and $\boldsymbol{u}_{\mathrm{i}_h} \in \boldsymbol{\mathcal{W}}_{\boldsymbol{u}}^{\mathrm{i}}([0,T], \boldsymbol{\mathcal{V}}_{\boldsymbol{u}_h}^{\mathrm{i}})$ such that

$$\frac{1}{\rho_0 c_0^2}(\partial_t p_{\mathrm{i}_h}, q_h) - \frac{1}{\rho_0 c_0^2}(\boldsymbol{u}_{\mathrm{dom}} \cdot \nabla p_{\mathrm{i}_h}, q_h) + (\nabla \cdot \boldsymbol{u}_{\mathrm{i}_h}, q_h)$$
$$+ \sum_{\Omega_{el}}(\tau_p \mathcal{P}\big[-\frac{1}{\rho_0 c_0^2}\boldsymbol{u}_{\mathrm{dom}} \cdot \nabla p_{\mathrm{i}_h} + \nabla \cdot \boldsymbol{u}_{\mathrm{i}_h} - Q\big], -\frac{1}{\rho_0 c_0^2}\boldsymbol{u}_{\mathrm{dom}} \cdot \nabla q_h + \nabla \cdot \boldsymbol{v}_h)_{\Omega_e(t)} = (Q^{n+1}, q_h), \quad (19a)$$

$$\rho_0(\partial_t \boldsymbol{u}_{\mathrm{i}_h}, \boldsymbol{v}_h) - \rho_0(\boldsymbol{u}_{\mathrm{dom}} \cdot \nabla \boldsymbol{u}_{\mathrm{i}_h}, \boldsymbol{v}_h) + (\nabla p_{\mathrm{i}_h}, \boldsymbol{v}_h)$$
$$+ \sum_{\Omega_{el}}(\tau_{\boldsymbol{u}} \mathcal{P}\big[-\rho_0 \boldsymbol{u}_{\mathrm{dom}} \cdot \nabla \boldsymbol{u}_{\mathrm{i}_h} + \nabla p_{\mathrm{i}_h} - \boldsymbol{f}\big], -\rho_0 \boldsymbol{u}_{\mathrm{dom}} \cdot \nabla \boldsymbol{v}_h + \nabla q_h)_{\Omega_e(t)} = (\boldsymbol{f}, \boldsymbol{v}_h), \quad (19b)$$

for all $q_h \in \mathcal{V}_{p_h}^{\mathrm{i}}$ and $\boldsymbol{v}_h \in \boldsymbol{\mathcal{V}}_{\boldsymbol{u}_h}^{\mathrm{i}}$. The first rows in equations (19a) and (19b) correspond to the Galerkin FEM terms, while the second rows contain the stabilizing ones. Notice that we have limited here to the case of quasi-static subscales for simplicity. $\Omega_{el}(t)$ represents a time evolving element of the FEM mesh. The operator $\mathcal{P}$ in (19) represents a projection that is applied to scalars or vectors depending on the argument. In the OSS FEM method $\mathcal{P} = \boldsymbol{I} - \Pi_h$, where $\boldsymbol{I}$ stands for the identity and Π_h for the L^2-projection onto the finite element space. In what concerns the stabilization parameters τ_p and $\tau_{\boldsymbol{u}}$ in (19a) and (19b), they are given by (see [38]),

$$\tau_{\boldsymbol{u}} = \frac{h}{C_1 \rho_0 |\boldsymbol{u}_h| + \rho_0 c_0 C_2}, \qquad \tau_p = \frac{\rho_0 c_0^2 h}{C_1 |\boldsymbol{u}_h| + c_0 C_2}, \qquad (20)$$

with C_1 and C_2 denoting constants obtained from numerical experiments. In [38], the following values were deemed appropriate for simulations using linear elements, $C_1 = C_2 = 100$.

As regards the diffraction problem in (18), its stabilized OSS FEM formulation consists in finding $p_{\mathrm{d}_h} \in \mathcal{W}_p^{\mathrm{d}}([0,T], \mathcal{V}_{p_h}^{\mathrm{d}})$ and $\boldsymbol{u}_{\mathrm{d}_h} \in \boldsymbol{\mathcal{W}}_{\boldsymbol{u}}^{\mathrm{d}}([0,T], \boldsymbol{\mathcal{V}}_{\boldsymbol{u}_h}^{\mathrm{d}})$ such that

$$\frac{1}{\rho_0 c_0^2}(\partial_t p_{\mathrm{d}_h}, q_h) - \frac{1}{\rho_0 c_0^2}(\boldsymbol{u}_{\mathrm{dom}} \cdot \nabla p_{\mathrm{d}_h}, q_h) + (\nabla \cdot \boldsymbol{u}_{\mathrm{d}_h}, q_h) - (q_h, \boldsymbol{u}_{\mathrm{d}_h} \cdot \boldsymbol{n})_{\Gamma_{\mathrm{b}}}$$
$$+ \sum_{\Omega_{el}}(\tau_p \mathcal{P}\big[-\frac{1}{\rho_0 c_0^2}\boldsymbol{u}_{\mathrm{dom}} \cdot \nabla p_{\mathrm{d}_h} + \nabla \cdot \boldsymbol{u}_{\mathrm{d}_h}\big], -\frac{1}{\rho_0 c_0^2}\boldsymbol{u}_{\mathrm{dom}} \cdot \nabla q_h + \nabla \cdot \boldsymbol{v}_h)_{\Omega_e(t)}$$
$$= -(q_h, (\boldsymbol{u}_{\mathrm{dom}} - \boldsymbol{u}_{\mathrm{i}_h}) \cdot \boldsymbol{n})_{\Gamma_{\mathrm{b}}} \qquad (21a)$$

$$\rho_0(\partial_t \boldsymbol{u}_{\mathrm{d}_h}, \boldsymbol{v}_h) - \rho_0(\boldsymbol{u}_{\mathrm{dom}} \cdot \nabla \boldsymbol{u}_{\mathrm{d}_h}, \boldsymbol{v}_h) - (\nabla \cdot \boldsymbol{v}_h, p_{\mathrm{d}_h}) + (\boldsymbol{v}_h \cdot \boldsymbol{n}, p_{\mathrm{d}_h})_{\Gamma_{\mathrm{b}}} + \alpha(\boldsymbol{v}_h, \boldsymbol{u}_{\mathrm{d}_h} \cdot \boldsymbol{n} - (\boldsymbol{u}_{\mathrm{dom}} - \boldsymbol{u}_{\mathrm{i}_h}) \cdot \boldsymbol{n})_{\Gamma_{\mathrm{b}}}$$
$$+ \sum_{\Omega_{el}}(\tau_{\boldsymbol{u}} \mathcal{P}\big[-\rho_0 \boldsymbol{u}_{\mathrm{dom}} \cdot \nabla \boldsymbol{u}_{\mathrm{d}_h} + \nabla p_{\mathrm{d}_h}\big], -\rho_0 \boldsymbol{u}_{\mathrm{dom}} \cdot \nabla \boldsymbol{v}_h + \nabla q_h)_{\Omega_e(t)} = 0, \qquad (21b)$$

for all $q_h \in \mathcal{V}_{p_h}^{\mathrm{d}}$ and $\boldsymbol{v}_h \in \boldsymbol{\mathcal{V}}_{\boldsymbol{u}_h}^{\mathrm{d}}$. Again, the first rows of (21a) and (21b) contain the Galerkin FEM terms, while the stabilization ones with parameters in (20) are provided in the second rows.

3.3. Final spatial and time numerical discretization

Once discretized in space, the FEM equations (19) and (21) must be discretized in time. To that purpose we divide the time interval $[0\ T]$ into N steps t^n, $n = 1 \ldots N$, with time step size $\Delta t = t^{n+1} - t^n$

and $t^1 = \Delta t$, $t^N = T$. For any arbitrary scalar g or vector $\boldsymbol{g}$ time-dependent functions, g^n and $\boldsymbol{g}^n$ will denote an approximation to their evaluation at time $t^n = n\Delta t$. For the examples in the current work, a second order backward differentiation formula (BDF2) will be used as an approximation to the first order time derivative of $g \equiv p$ and $\boldsymbol{g} \equiv \boldsymbol{u}$, so that $dg/dt\big|_{t^n} \approx \delta_t g^{n+1} := (1/2\Delta t)(3g^{n+1} - 4g^n + g^{n-1})$. The FEM time discrete formulation of the incident wave acoustic problem (19) is therefore given by

$$
\begin{aligned}
&\frac{1}{\rho_0 c_0^2}(\delta_t p_{\mathrm{i}_h}^{n+1}, q_h) - \frac{1}{\rho_0 c_0^2}(\boldsymbol{u}_{\mathrm{dom}} \cdot \nabla p_{\mathrm{i}_h}^{n+1}, q_h) + (\nabla \cdot \boldsymbol{u}_{\mathrm{i}_h}^{n+1}, q_h) \\
&+ \sum_{\Omega_{el}} (\tau_p \mathcal{P}\big[- \frac{1}{\rho_0 c_0^2}\boldsymbol{u}_{\mathrm{dom}} \cdot \nabla p_{\mathrm{i}_h}^{n+1} + \nabla \cdot \boldsymbol{u}_{\mathrm{i}_h}^{n+1} - Q^{n+1}\big], -\frac{1}{\rho_0 c_0^2}\boldsymbol{u}_{\mathrm{dom}} \cdot \nabla q_h + \nabla \cdot \boldsymbol{v}_h)_{\Omega_e(t^n)} = (Q^{n+1}, q_h),
\end{aligned}
\tag{22a}
$$

$$
\begin{aligned}
&\rho_0(\delta_t \boldsymbol{u}_{\mathrm{i}_h}^{n+1}, \boldsymbol{v}_h) - \rho_0(\boldsymbol{u}_{\mathrm{dom}} \cdot \nabla \boldsymbol{u}_{\mathrm{i}_h}^{n+1}, \boldsymbol{v}_h) + (\nabla p_{\mathrm{i}_h}^{n+1}, \boldsymbol{v}_h) \\
&+ \sum_{\Omega_{el}} (\tau_{\boldsymbol{u}} \mathcal{P}\big[- \rho_0 \boldsymbol{u}_{\mathrm{dom}} \cdot \nabla \boldsymbol{u}_{\mathrm{i}_h}^{n+1} + \nabla p_{\mathrm{i}_h}^{n+1} - \boldsymbol{f}^{n+1}\big], -\rho_0 \boldsymbol{u}_{\mathrm{dom}} \cdot \nabla \boldsymbol{v}_h + \nabla q_h)_{\Omega_e(t^n)} = (\boldsymbol{f}^{n+1}, \boldsymbol{v}_h).
\end{aligned}
\tag{22b}
$$

Observe that $\mathcal{P}(\delta_t p_h) = 0$ and $\mathcal{P}(\delta_t \boldsymbol{u}_h) = 0$ in (22) because we are dealing with orthogonal subscales.

Analogously, the FEM time discrete version of the diffraction wave problem (21) reads,

$$
\begin{aligned}
&\frac{1}{\rho_0 c_0^2}(\delta_t p_{\mathrm{d}_h}^{n+1}, q_h) - \frac{1}{\rho_0 c_0^2}(\boldsymbol{u}_{\mathrm{dom}} \cdot \nabla p_{\mathrm{d}_h}^{n+1}, q_h) + (\nabla \cdot \boldsymbol{u}_{\mathrm{d}_h}^{n+1}, q_h) - (q_h, \boldsymbol{u}_{\mathrm{d}_h}^{n+1} \cdot \boldsymbol{n})_{\Gamma_{\mathrm{b}}} \\
&+ \sum_{\Omega_{el}} (\tau_p \mathcal{P}\big[- \frac{1}{\rho_0 c_0^2}\boldsymbol{u}_{\mathrm{dom}} \cdot \nabla p_{\mathrm{d}_h}^{n+1} + \nabla \cdot \boldsymbol{u}_{\mathrm{d}_h}^{n+1}\big], -\frac{1}{\rho_0 c_0^2}\boldsymbol{u}_{\mathrm{dom}} \cdot \nabla q_h + \nabla \cdot \boldsymbol{v}_h)_{\Omega_e(t^n)} \\
&= - \big(q_h, \big(\boldsymbol{u}_{\mathrm{dom}} - \boldsymbol{u}_{\mathrm{i}_h}^{n+1}\big) \cdot \boldsymbol{n}\big)_{\Gamma_{\mathrm{b}}},
\end{aligned}
\tag{23a}
$$

$$
\begin{aligned}
&\rho_0(\delta_t \boldsymbol{u}_{\mathrm{d}_h}^{n+1}, \boldsymbol{v}_h) - \rho_0(\boldsymbol{u}_{\mathrm{dom}} \cdot \nabla \boldsymbol{u}_{\mathrm{d}_h}^{n+1}, \boldsymbol{v}_h) - (\nabla \cdot \boldsymbol{v}_h, p_{\mathrm{d}_h}^{n+1}) + (\boldsymbol{v}_h \cdot \boldsymbol{n}, p_{\mathrm{d}_h}^{n+1})_{\Gamma_{\mathrm{b}}} \\
&+ \alpha(\boldsymbol{v}_h, \boldsymbol{u}_{\mathrm{d}_h}^{n+1} \cdot \boldsymbol{n} - \big(\boldsymbol{u}_{\mathrm{dom}} - \boldsymbol{u}_{\mathrm{i}_h}^{n+1}\big) \cdot \boldsymbol{n})_{\Gamma_{\mathrm{b}}} \\
&+ \sum_{\Omega_{el}} (\tau_{\boldsymbol{u}} \mathcal{P}\big[- \rho_0 \boldsymbol{u}_{\mathrm{dom}} \cdot \nabla \boldsymbol{u}_{\mathrm{d}_h}^{n+1} + \nabla p_{\mathrm{d}_h}^{n+1}\big], -\rho_0 \boldsymbol{u}_{\mathrm{dom}} \cdot \nabla \boldsymbol{v}_h + \nabla q_h)_{\Omega_e(t^n)} = 0.
\end{aligned}
\tag{23b}
$$

4. Unified flow and acoustics isentropic compressible solver in an ALE frame of reference

4.1. Problem statement: the differential continuous problem

As explained in the Introduction, the CAA method proposed in the previous section belongs to the group of hybrid CAA strategies, which segregate the flow dynamics and the acoustic problems. In this work, the total acoustic pressure computed in this way will be compared with that from a DNC CAA computation. In particular, we will resort to the DNC isentropic compressible flow equations in primitive variables presented by the authors in [7], which is set herein in an ALE framework. The formulation in [7] consists of a unified solver for the continuity and momentum conservation equations for the compressible velocity and pressure fields. It can be applied to a large number of gas flow problems in the subsonic regime. The isentropic assumption allows one to get rid of the energy conservation equation and drastically reduces the computational cost if compared to that of a fully compressible approach (see e.g., [48, 63]). The result is a solver which converges to a DNC in the low Mach number regime and reduces the complexity gap between the compressible formulations and the hybrid ones in computational aeroacoustics. As said in the Introduction, a monolithic scheme will be used for the isentropic compressible flow problem in this paper, though, recently, a fractional step method has been derived for it [40].

Unlike hybrid approaches, there is no separation here between the acoustic and the Navier-Stokes computational domains in Fig.1. The isentropic compressible equations must be solved in the whole acoustic

domain $\Omega_{\text{ac}}(t)$ using an ALE frame of reference. Our goal is that of finding the compressible velocity $\boldsymbol{u}^c$ and pressure p^c that satisfy the non-linear equations

$$\frac{1}{\rho c^2}\frac{\partial p^c}{\partial t} + \frac{1}{\rho c^2}\left(\boldsymbol{u}^c - \boldsymbol{u}_{\text{dom}}\right)\cdot\nabla p^c + \nabla\cdot\boldsymbol{u}^c = Q \quad \text{in } \Omega_{\text{ac}}(t),\ t>0, \tag{24a}$$

$$\rho\frac{\partial\boldsymbol{u}^c}{\partial t} + \rho\left(\boldsymbol{u}^c - \boldsymbol{u}_{\text{dom}}\right)\cdot\nabla\boldsymbol{u}^c - \mu\Delta\boldsymbol{u}^c - \frac{1}{3}\mu\nabla(\nabla\cdot\boldsymbol{u}^c) + \nabla p^c = \boldsymbol{f} \quad \text{in } \Omega_{\text{ac}}(t),\ t>0, \tag{24b}$$

where μ is the dynamic viscosity. In addition to $\boldsymbol{u}^c$ and p^c, these equations contain as unknowns the speed of sound $c(\boldsymbol{x},t)$ and the density $\rho(\boldsymbol{x},t)$, so they need to be closed. This is done by taking,

$$\rho = \rho_0\left(1 + \frac{\gamma-1}{2}\text{M}^2\right)^{\frac{-1}{\gamma-1}}, \tag{25a}$$

$$c^2 = c_0^2\left(1 + \frac{\gamma-1}{2}\text{M}^2\right)^{-1}, \tag{25b}$$

with γ being the adiabatic constant of the gas and $\text{M} = |\boldsymbol{u}^c|/c_0$ the local Mach number.

Equations (24) plus (25) are to be supplemented with appropriate initial and boundary conditions. In fact, imposing boundary conditions on Γ_∞, which, as seen in Fig. 1, has been split into $\Gamma_\infty = \Gamma_{\text{Li}} \cup \Gamma_{\text{Lu}} \cup \Gamma_{\text{Ld}} \cup \Gamma_{\text{O}}$ (with null intersection between them and with $\boldsymbol{u}_{\text{dom}} = \boldsymbol{0}$ on Γ_∞), constitutes the main difficulty of the method (stabilization FEM issues aside). While in a CFD simulation one would typically prescribe an inlet velocity at Γ_{Li}, a zero normal velocity component at Γ_{Lu} and Γ_{Ld}, and no traction at Γ_{O}, such conditions do not prevent reflections from the aeroacoustic waves at the boundary Γ_∞. As explained in [7], the strategy to avoid this problem and allow acoustic waves propagate towards infinity is to perform a decomposition of the computed compressible velocity $\boldsymbol{u}^c$ and pressure p^c fields into mean and acoustic components, and impose different boundary conditions on them. We get,

$$\boldsymbol{u}^c\left(\boldsymbol{x},t\right) = \bar{\boldsymbol{u}}\left(\boldsymbol{x},t\right) + \boldsymbol{u}\left(\boldsymbol{x},t\right), \tag{26a}$$

$$p^c\left(\boldsymbol{x},t\right) = \bar{p}\left(\boldsymbol{x},t\right) + p\left(\boldsymbol{x},t\right), \tag{26b}$$

where $\bar{\boldsymbol{u}}$ and $\bar{p}$ denote the mean quantities and $\boldsymbol{u}$ and p, the acoustic ones (according to the notation in section 3). The mean components are obtained by low-pass filtering $\boldsymbol{u}^c$ and p^c, i.e.,

$$\bar{\boldsymbol{u}} = T_w^{-1}\int_{t-T_w}^t \boldsymbol{u}^c(\boldsymbol{x},s)ds, \qquad \bar{p} = T_w^{-1}\int_{t-T_w}^t p^c(\boldsymbol{x},s)ds \tag{27}$$

where T_w is the time window that determines the cut-off frequency. It is to be noted that if viscosity was ignored and the mean velocity was set to zero, substitution of (26) into (24) would recover equation (11), after linearization.

The boundary conditions on $\Gamma_\infty = \Gamma_{\text{Li}} \cup \Gamma_{\text{Lu}} \cup \Gamma_{\text{Ld}} \cup \Gamma_{\text{O}}$ are set as follows. On Γ_{Li}, Γ_{Lu} and Γ_{Ld} we impose standard Dirichlet conditions for $\bar{\boldsymbol{u}}$ but mixed conditions (normal component and tangent stress) for the acoustic velocity $\boldsymbol{u}$. On Γ_{O}, we prescribe Neumann boundary conditions for $\bar{\boldsymbol{u}}$ (no traction) and again mixed conditions for $\boldsymbol{u}$. All conditions on Γ_{Li}, Γ_{Lu}, Γ_{Ld} and Γ_{O} will be weakly imposed in the variational formulation of the problem (see next section). As regards the body surface $\Gamma_{\text{b}}(t)$, it is considered to be rigid so the compressible velocity $\boldsymbol{u}^c$ will vanish there and the velocity at the boundary will be that of the moving mesh $\boldsymbol{u}_{\text{dom}}$. The initial and boundary conditions that complete equations (24) are therefore given by (see Fig. 1),

$$\boldsymbol{u}^c\left(\boldsymbol{x},0\right) = \boldsymbol{u}_0^c\left(\boldsymbol{x}\right) \quad \text{in } \Omega_{\text{ac}}(t),\ t=0, \tag{28a}$$

$$\boldsymbol{u}^c\left(\boldsymbol{x},t\right) = \boldsymbol{u}_{\text{dom}}\left(\boldsymbol{x},t\right) \quad \text{on } \Gamma_{\text{b}}(t),\ t>0, \tag{28b}$$

$$\bar{\boldsymbol{u}}\left(\boldsymbol{x},t\right) = \boldsymbol{u}_{\text{Li}} \quad \text{on } \Gamma_{\text{Li}},\ t>0, \tag{28c}$$

$$\boldsymbol{n}\cdot\boldsymbol{u} = -\frac{1}{\rho_0 c_0}\boldsymbol{n}\cdot\left[\boldsymbol{n}\cdot\boldsymbol{\sigma}\left(\boldsymbol{u},p\right)\right] \quad \text{on } \Gamma_{\text{Li}},\ t>0, \tag{28d}$$

$$\boldsymbol{m} \cdot [\boldsymbol{n} \cdot \boldsymbol{\sigma}\left(\boldsymbol{u}, p\right)] = 0 \quad \text{on } \Gamma_{\text{Li}}, \ t > 0, \tag{28e}$$

$$\boldsymbol{n} \cdot \bar{\boldsymbol{u}}\left(\boldsymbol{x}, t\right) = 0 \quad \text{on } \Gamma_{\text{Lu}} \cup \Gamma_{\text{Ld}}, \ t > 0, \tag{28f}$$

$$\boldsymbol{n} \cdot \boldsymbol{u} = -\frac{1}{\rho c} \boldsymbol{n} \cdot [\boldsymbol{n} \cdot \boldsymbol{\sigma}\left(\boldsymbol{u}, p\right)] \quad \text{on } \Gamma_{\text{Lu}} \cup \Gamma_{\text{Ld}}, \ t > 0, \tag{28g}$$

$$\boldsymbol{m} \cdot [\boldsymbol{n} \cdot \boldsymbol{\sigma}\left(\boldsymbol{u}, p\right)] = 0 \quad \text{on } \Gamma_{\text{Lu}} \cup \Gamma_{\text{Ld}}, \ t > 0, \tag{28h}$$

$$\boldsymbol{n} \cdot \boldsymbol{\sigma}\left(\bar{\boldsymbol{u}}, \bar{p}\right) = \mathbf{0} \quad \text{on } \Gamma_O, \ t > 0, \tag{28i}$$

$$\boldsymbol{n} \cdot \boldsymbol{u} = -\frac{1}{\rho c} \boldsymbol{n} \cdot [\boldsymbol{n} \cdot \boldsymbol{\sigma}\left(\boldsymbol{u}, p\right)] \quad \text{on } \Gamma_O, \ t > 0, \tag{28j}$$

$$\boldsymbol{m} \cdot [\boldsymbol{n} \cdot \boldsymbol{\sigma}\left(\boldsymbol{u}, p\right)] = 0 \quad \text{on } \Gamma_O, \ t > 0, \tag{28k}$$

where $\boldsymbol{\sigma}(\boldsymbol{u}^c, p^c) = -p^c \boldsymbol{I} + \mu \nabla \boldsymbol{u}^c + \frac{1}{3}\mu\left(\nabla \cdot \boldsymbol{u}^c\right) \boldsymbol{I}$ stands for the the stress tensor, $\boldsymbol{I}$ being the identity and $\boldsymbol{n}$ and $\boldsymbol{m}$ the normal and tangent vectors to a boundary. The mesh velocity $\boldsymbol{u}_{\text{dom}}$ vanishes at Γ_∞. It is to be noted that in the case of an inviscid flow ($\mu = 0$), the condition on the tangent component of the acoustic velocities at Γ_∞ (equations (28e), (28h) and (28k)) vanishes as one could expect, and that for the normal component (equations (28d), (28g) and (28j)) reduces to the well-known Sommerfeld's radiation condition for acoustic waves, $p = \rho c\left(\boldsymbol{u} \cdot \boldsymbol{n}\right)$. In what follows and to condensate the notation, we will unify the boundaries $\Gamma_{\text{Li}} \cup \Gamma_{\text{Lu}} \cup \Gamma_{\text{Ld}} =: \Gamma_{\text{L}}$ so that $\bar{\boldsymbol{u}}_L$ will generally designate the different mean values assigned to the subsets of Γ_{L} (remember that $\boldsymbol{u}_{\text{dom}} = \mathbf{0}$ on Γ_{L}). The same will hold true for the conditions for the acoustic velocity $\boldsymbol{u}$ on Γ_{L}.

4.2. Weak formulation of the ALE isentropic compressible flow problem

For the FEM approximation of problem (24) we first need to get its variational formulation. To that goal we multiply (24a) by a scalar test function q and (24b) by a vector test function $\boldsymbol{v}$, and then integrate over the computational domain. After integration by parts and application of the boundary conditions, we are left with the weak form we were looking for. Two points are to be noted. The first one concerns notation. In order to get more compact expressions, all terms involving the problem unknowns and integration over the computational domain $\Omega_{\text{ac}}(t)$ will be grouped in a semilinear form $B([\boldsymbol{u}^c, p^c], [\boldsymbol{v}, q])$, while terms involving the problem unknowns and integration on the boundary Γ_∞ will be collected in a bilinear form $B_B([\boldsymbol{u}^c, p^c], [\boldsymbol{v}, q])$. Concerning the later, it shall be mentioned that to make the boundary conditions for the acoustic and mean components compatible, they all have to be prescribed in weak form. To impose the Dirichlet conditions $\bar{\boldsymbol{u}} = \boldsymbol{u}_{\text{L}}$ weakly, we therefore resort again to penalization using Nitsche's method [50], which demands symmetry of the boundary terms. The rigidity condition on the moving body surface $\Gamma_{\text{b}}(t)$ is imposed strongly. Finally, problem data involving known boundary values and/or external forces and volume sources are grouped in a linear form $L_B(\boldsymbol{v}, q)$ (in what follows we take $\boldsymbol{f} = \mathbf{0}$ and $Q = 0$). The expressions for $B([\boldsymbol{u}^c, p^c], [\boldsymbol{v}, q])$, $B_B([\boldsymbol{u}^c, p^c], [\boldsymbol{v}, q])$ and $L_B(\boldsymbol{v}, q)$ are given by,

$$B\left([\boldsymbol{u}^c, p^c], [\boldsymbol{v}, q]\right) = \left(\rho\boldsymbol{v}, \frac{\partial \boldsymbol{u}^c}{\partial t}\right) + \left(\rho\boldsymbol{v}, [(\boldsymbol{u}^c - \boldsymbol{u}_{\text{dom}}) \cdot \nabla]\,\boldsymbol{u}^c\right) + \mu\left(\nabla\boldsymbol{v}, \nabla\boldsymbol{u}^c\right) \tag{29a}$$

$$+ \frac{1}{3}\mu\left(\nabla \cdot \boldsymbol{v}, \nabla \cdot \boldsymbol{u}^c\right) - \left(\nabla \cdot \boldsymbol{v}, p^c\right) + \left(\frac{1}{\rho c^2}q, \frac{\partial p^c}{\partial t}\right) + \left(\frac{1}{\rho c^2}q, (\boldsymbol{u}^c - \boldsymbol{u}_{\text{dom}}) \cdot \nabla p^c\right) + \left(q, \nabla \cdot \boldsymbol{u}^c\right),$$

$$B_B\left([\boldsymbol{u}^c, p^c], [\boldsymbol{v}, q]\right) := -\left(\boldsymbol{v}, \boldsymbol{n} \cdot \boldsymbol{\sigma}\left(\bar{\boldsymbol{u}}, \bar{p}\right)\right)_{\Gamma_{\text{L}}} - \left(\bar{\boldsymbol{u}}, \boldsymbol{n} \cdot \boldsymbol{\sigma}\left(\boldsymbol{v}, q\right)\right)_{\Gamma_{\text{L}}} + \beta\frac{\mu_p}{l_p}\left(\boldsymbol{v}, \bar{\boldsymbol{u}}\right)_{\Gamma_{\text{L}}} \tag{29b}$$

$$+ \left(\rho c\boldsymbol{v} \cdot \boldsymbol{n}, \boldsymbol{u} \cdot \boldsymbol{n}\right)_{\Gamma_{\text{L}}} + \left(\rho c\boldsymbol{v} \cdot \boldsymbol{n}, \boldsymbol{u} \cdot \boldsymbol{n}\right)_{\Gamma_O},$$

$$L_{\text{B}}\left([\boldsymbol{v}, q]\right) := -\left(\boldsymbol{u}_{\text{L}} + \boldsymbol{u}_{\text{dom}}, \boldsymbol{n} \cdot \boldsymbol{\sigma}\left(\boldsymbol{v}, q\right)\right)_{\Gamma_{\text{L}}} + \beta\frac{\mu_p}{l_p}\left(\boldsymbol{v}, \boldsymbol{u}_L\right)_{\Gamma_{\text{L}}}, \tag{29c}$$

where β, μ_p, l_p are numerical parameters to be determined. The first one is dimensionless, the second one has units of viscosity and the third has length units.

With the above identifications, the variational isentropic compressible problem can be posed as that of finding $p^c \in \mathcal{W}_p^c([0, T], \mathcal{V}_p^c)$ and $\boldsymbol{u}^c \in \boldsymbol{\mathcal{W}}_{\boldsymbol{u}}^c([0, T], \boldsymbol{\mathcal{V}}_{\boldsymbol{u}}^c)$ such that

$$B\left([\boldsymbol{u}^c, p^c], [\boldsymbol{v}, q]\right) + B_B\left([\boldsymbol{u}^c, p^c], [\boldsymbol{v}, q]\right) = L_{\text{B}}\left([\boldsymbol{v}, q]\right) \tag{30}$$

for all $q \in \mathcal{V}_p^c$ and $\boldsymbol{v} \in \boldsymbol{\mathcal{V}}_{\boldsymbol{u}}^c$. Again, $\mathcal{W}_p^c$, $\boldsymbol{\mathcal{W}}_{\boldsymbol{u}}^c$, $\mathcal{V}_p^c$ and $\boldsymbol{\mathcal{V}}_{\boldsymbol{u}}^c$ designate appropriate functional spaces not to be detailed herein. The variational problem (30) is essentially that in [7] except for the mesh velocity that affects the convective terms and the boundary conditions.

4.3. Fully discrete problem for the ALE isentropic compressible flow problem

Full details on the FEM space and finite difference time discretization of the non-ALE counterpart of (30) can be found in [7], so we will only succinctly describe how to get a fully discrete scheme for the ALE one in this section, due to the close similarity. As for the FEM space discretization, we start finding finite element spaces $\mathcal{V}_{ph}^c \subset \mathcal{V}_p^c$ and $\boldsymbol{\mathcal{V}}_{\boldsymbol{u}h}^c \subset \boldsymbol{\mathcal{V}}_{\boldsymbol{u}}^c$ such that the approximate FEM compressible flow velocity $\boldsymbol{u}_h^c$ and pressure p_h^c (as well as their corresponding test functions) can be expressed as a linear combination of the bases spanning $\mathcal{V}_{ph}^c$ and $\boldsymbol{\mathcal{V}}_{\boldsymbol{u}h}^c$. On the other hand, as we are dealing with a mixed problem, stabilization is required if we want to use the same interpolation for the compressible velocity and pressure fields [54]. Concerning the time dicretization, we use a BDF2 time integrator, like in section 3.3. The fully discrete variational version of (30) consists in solving, at time step t^{n+1},

$$B^{n+1}([\boldsymbol{u}_h^c, p_h^c], [\boldsymbol{v}_h, q_h]) + B_B^{n+1}([\boldsymbol{u}_h^c, p_h^c], [\boldsymbol{v}_h, q_h]) + B_S^{n+1}([\boldsymbol{u}_h^c, p_h^c], [\boldsymbol{v}_h, q_h]) = L_B^{n+1}([\boldsymbol{v}_h, q_h]), \qquad (31)$$

where $B_S^{n+1}([\boldsymbol{u}_h^c, p_h^c], [\boldsymbol{v}_h, q_h])$ is the semilinear form for the stabilization terms, to be detailed below, and $B^{n+1}([\boldsymbol{u}_h^c, p_h^c], [\boldsymbol{v}_h, q_h])$, $B_B^{n+1}([\boldsymbol{u}_h^c, p_h^c], [\boldsymbol{v}_h, q_h])$ and $L_B^{n+1}([\boldsymbol{v}_h, q_h])$ are the discrete, straightforward counterparts of (29a), (29b) and (29c). Before introducing $B_S^{n+1}([\boldsymbol{u}_h^c, p_h^c], [\boldsymbol{v}_h, q_h])$, let us draw our attention to some general aspects of (31). When expressed in matrix form, the sole unknowns of the problem must be $\boldsymbol{u}_h^c$ and p_h^c. All other variables in (31) shall be written in terms of them. As for the density, ρ, and the speed of sound, c, (see (29a) and (29b)), this can be done through equations (25a) and (25b), by computing the local Mach number in terms of $\boldsymbol{u}_h^c$. The situation is more intricate for the discrete mean, $\bar{\boldsymbol{u}}_h$, $\bar{p}_h$ and acoustic, $\boldsymbol{u}_h$, p_h quantities in $B_B^{n+1}([\boldsymbol{u}_h^c, p_h^c], [\boldsymbol{v}_h, q_h])$, arising from (29b). In this case one can relate them to $\boldsymbol{u}_h^c$ and p_h^c once the filter operation in (27) has been discretized using a trapezoidal rule. As regards the constants β, μ_p and l_p in $B_B^{n+1}([\boldsymbol{u}_h^c, p_h^c], [\boldsymbol{v}_h, q_h])$ and $L_B^{n+1}([\boldsymbol{v}_h, q_h])$, they can be taken as $\beta = 1$, $\mu_p = \mu + \rho|\boldsymbol{u}_h^c|/h$, and $l_p = h$ (see [64]).

In what concerns the stabilization term $B_S^{n+1}([\boldsymbol{u}_h^c, p_h^c], [\boldsymbol{v}_h, q_h])$ in (31), this has been obtained from an algebraic subgrid scale approach (ASGS) [65], which yields,

$$
\begin{aligned}
&B_S^{n+1}([\boldsymbol{u}_h^c, p_h^c], [\boldsymbol{v}_h, q_h]) \\
&= \sum_{\Omega_{el}} \tau_{1,el}((\rho\boldsymbol{u}_h^{c,n+1} - \boldsymbol{u}_{\text{dom}}) \cdot \nabla\boldsymbol{v}_h + \nabla q_h, \rho\delta_t\boldsymbol{u}_h^{c,n+1} + \rho(\boldsymbol{u}_h^{c,n+1} - \boldsymbol{u}_{\text{dom}}) \cdot \nabla\boldsymbol{u}_h^{c,n+1} - \nabla \cdot \boldsymbol{\sigma}_h^{n+1})_{\Omega_{el}} \\
&+ \sum_{\Omega_{el}} \tau_{2,el}(\nabla \cdot \boldsymbol{v}_h + \frac{1}{\rho c^2}(\boldsymbol{u}_h^{c,n+1} - \boldsymbol{u}_{\text{dom}}) \cdot \nabla q_h, \nabla \cdot \boldsymbol{u}_h^{c,n+1} + \frac{1}{c^2}(\boldsymbol{u}_h^{c,n+1} - \boldsymbol{u}_{\text{dom}}) \cdot \nabla p_h^{c,n+1} + \frac{1}{\rho c^2}\delta_t p_h^{c,n+1})_{\Omega_{el}},
\end{aligned}
$$
$$(32)$$

where $\tau_{1,el}$ and $\tau_{2,el}$ are suitable stabilization parameters defined in each element [55]. These are obtained as,

$$\tau_{1,el} = \left[c_1\frac{\mu}{h^2} + c_2\rho\frac{|\boldsymbol{u}_h^{c,n+1} - \boldsymbol{u}_{\text{dom}}|_{\Omega_{el}}}{h} \right]^{-1}, \qquad \tau_{2,el} = \frac{h^2}{c_1\tau_{1,el}}, \qquad (33)$$

with $|\boldsymbol{u}_h^{c,n+1}|_{\Omega_{el}}$ standing for the mean Euclidean norm of the velocity in the element Ω_{el}. The constants c_1 and c_2 depend on the polynomial order of the interpolation and are set to $c_1 = 4$ and $c_2 = 2$ for linear elements. The reader is referred to [7] for a more detailed explanation on the choices for the discretization scheme presented in this section.
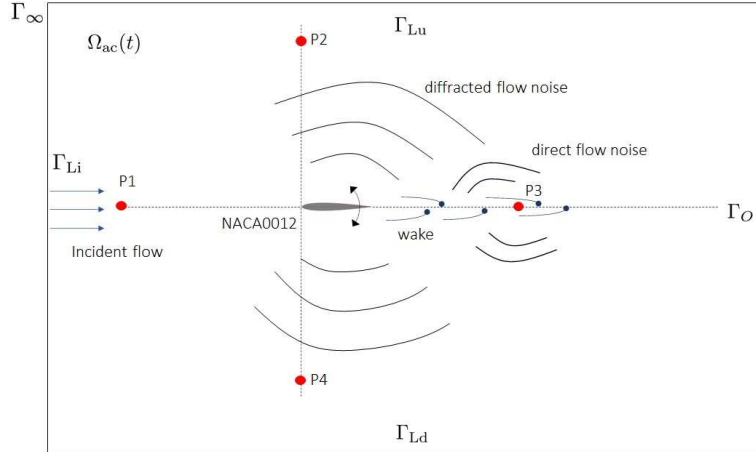
14

Figure 2: Sketch of the pitching NACA0012 airfoil aeroacoustic problem addressed with the hybrid splitting CAA strategy and the isentropic compressible solver. Location of the control points P1, P2, P3 and P4.

5. Numerical examples

To illustrate the performance of the ALE hybrid splitting CAA strategy of section 3 and the ALE direct isentropic compressible one in section 4, two numerical examples will be presented down below. The first one addresses the noise generated by flow past a two-dimensional NACA0012 airfoil that is oscillating with the center of rotation (pitching axis) located at its leading edge. The second example is also two-dimensional and consists of computing the sound generated by flow past a teeth-shaped object at a duct termination, which opens progressively. The motion of the airfoil and of the duct closure is prescribed resulting in a deformation of the FEM mesh. That is accounted for by solving an associated elastic problem for the displacament of the mesh nodes, as exposed in [66]. Given that the mesh distortion is not very high for the current examples, this strategy avoids the need of remeshing, which significantly reduces the computational cost. All units in the next sections are in SI, so we will not explicitly specify them.

5.1. Aeroacoustics of a slow oscillating 2D NACA0012 airfoil at $M = 0.1$

The first example consists of flow impinging on a two-dimensional NACA 0012 airfoil, which has an initial angle of attack of $\gamma = 5°$ [67], see Fig. 2. The Reynolds number based on the incident flow speed and airfoil chord ($c = 0.1524$) is $\text{Re}_c = 2.08 \times 10^5$, whereas the Mach number is $M = 0.2$. The airfoil pitches around the leading edge, where we place the origin of coordinates, with an angular frequency of $\omega_a = 40$. This is much lower than the frequency of the shed vortices for the static airfoil, which turns to be $\omega_s \sim 1.35 \times 10^4$, as demanded for the correct characterization of the quasi-stationary diffraction problem. Departing from the initial value $\gamma = 5°$, the angle of attack decreases to zero and keeps diminishing until the trailing edge reaches its maximum height corresponding to $\gamma_{\min} = -1.5°$. Then, γ starts increasing, passes through zero, and reaches its maximum value (minimum height of the trailing edge) at $\gamma_{\max} = 10.5°$. Note that the oscillation is not symmetric.

The computational domain has dimensions 1.5×1.5 and has been discretized with an unstructured mesh of nearly 6×10^5 linear elements, using equal interpolation spaces for the velocity and pressure fields. The mesh size is $h \sim 4 \times 10^{-5}$ on the airfoil surface $\Gamma_b(t)$. The case has been ran up to a time of $T = 0.045$, with a time step of $\Delta t = 10^{-5}$, starting from an initial incompressible solution to ease the initial convergence of the solver. As said before, the mesh deformation due to the airfoil motion has been computed following the approach in [66] and its velocity has been accounted for in the flow dynamics and the acoustics by means of the ALE formulations in sections 3 and 4. The prescription of the Dirichlet boundary condition (16c) for the diffracted problem on the airfoil surface in a weak sense, using Nitsche's method, has turned to be one of the most important features for numerical convergence. The penalty parameter in (18b) must be very high ($\sim 10^5$) to prevent mass losses.
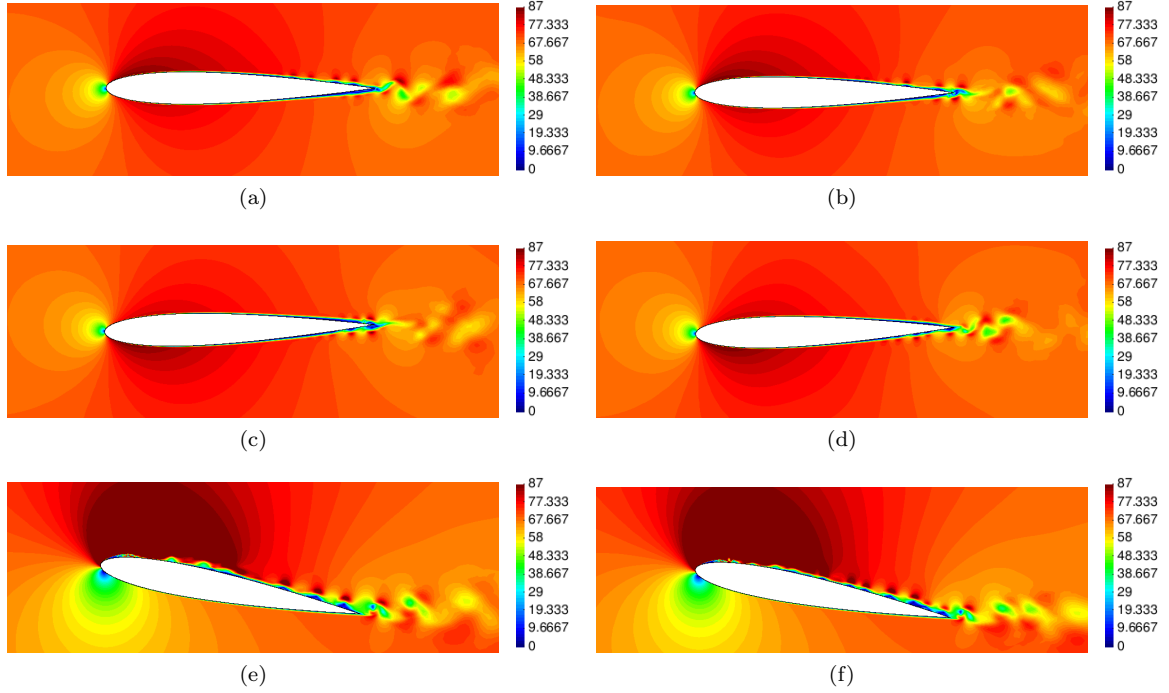
15

Figure 3: Zoomed snapshots of the incompressible (left column) and isentropic compressible (right column) velocity profiles for three different angles of attack: $\gamma_0 = 0°$ (first row), $\gamma_{\min} = -1.5°$ (second row) and $\gamma_{\max} = 10.5°$ (third row).

In Figs. 3 and 4 we first present results for the flow dynamics. The snaphshots in Fig. 3 correspond to velocity isosurfaces at different angles of attack. The first row shows the results for γ_0 (corresponding to $\gamma = 0°$), the second row for $\gamma_{\min}$ and the third one for $\gamma_{\max}$. The plots in the first column display the incompressible velocity around the airfoil computed in the first step of the hybrid CAA approach in section 3, while the second column contains plots for the compressible velocity calculated with the formulation in section 4. The results in the two columns of the figures are very close indicating that the isentropic compressible formulation correctly reproduces the nearly incompressible behaviour of the flow (though one should bear in mind that these are velocity profiles at a given instant). In Figs. 3a and b it is observed for γ_0 how the boundary layer slightly first detaches from the upper surface and how vortices are shed at the airfoil trailing edge. As opposed, for $\gamma_{\min}$ the boundary layer starts detaching from the lower surface. The oscillation of the airfoil perturbs the periodicity of the vortex shedding and one may find aperiodic patterns for the velocity (see e.g., Fig. 3c), from time to time. In the case of $\gamma_{\max}$, strong changes are appreciated. The boundary layer detaches from the upper surface but now at a point very close to the leading edge, which results in vortices travelling all over the airfoil upper surface and on larger and more intense vortex shedding at the trailing edge. As it will be shown below, that would have great impact on the generated aeroacoustic noise.

In Fig. 4, analogous results to those in Fig. 3 are presented, but now for the pressure. Each row in the figure respectively corresponds to angles of attack γ_0, $\gamma_{\min}$ and $\gamma_{\max}$. The plots in the first column show the incompressible pressure obtained from the incompressible Navier-Stokes equations, whereas the second column depicts the compressible pressure from the unified isentropic compressible solver. Both pressure fields would look very similar in the vicinity of the airfoil (as happened with the velocity in Fig. 3), but what it is interesting here is to check what occurs at the far field. Therefore, the pressure distribution over the whole computational domain is plotted in Fig. 4, instead of the zoom used for Fig. 3. As regards the results in the first column, it should be noted that the fluctuations in Figs. 4a, c and e are not acoustic waves propagating with the sound speed but incompressible pressure fluctuations. These fluctuations do
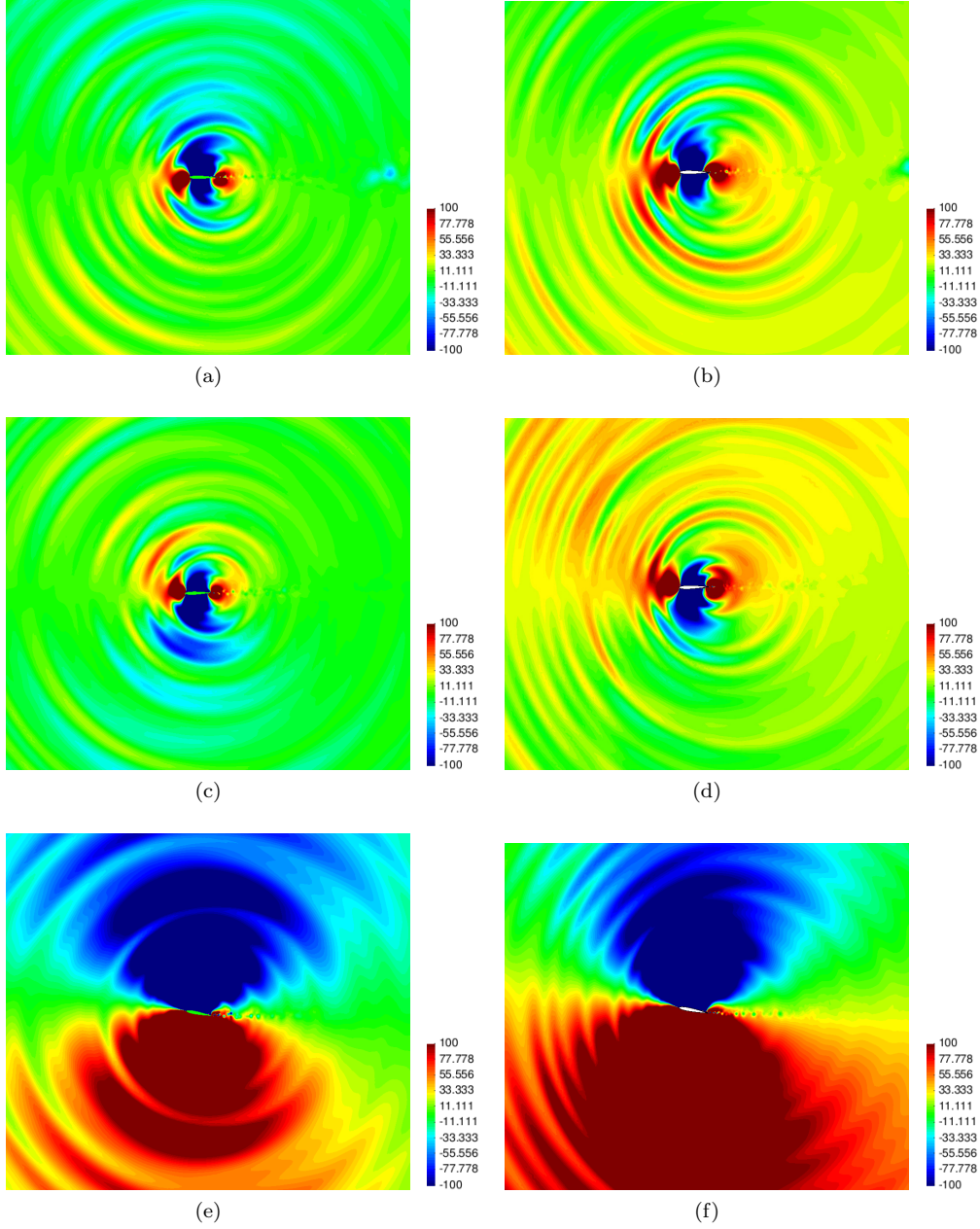
16

Figure 4: Snapshots of the incompressible (left column) and isentropic compressible (right column) pressure profiles for three different angles of attack: $\gamma_0 = 0°$ (first row), $\gamma_{\min} = -1.5°$ (second row) and $\gamma_{\max} = 10.5°$ (third row).

not satisfy an acoustic wave equation. As opposed, the pressure fluctuations at the far field in the second column of the figure do correspond to acoustic waves propagating outwards. If we compare the plots in the two columns, the results are significantly different, both in intensity and in separation between the extreme values of the fluctuations (which, as said, correspond to acoustic wavelengths for the compressible case). It is also apparent from the simulations that the acoustic field has a dipole pattern and that for $\gamma_{\max}$ the pressure variations are more intense than for γ_0 and $\gamma_{\min}$ (see Figs. 4b, d and f), which was expected given than the absolute value of $\gamma_{\max}$ is much higher than that of $\gamma_{\min}$ (rememeber that the oscillations are not symmetric

17
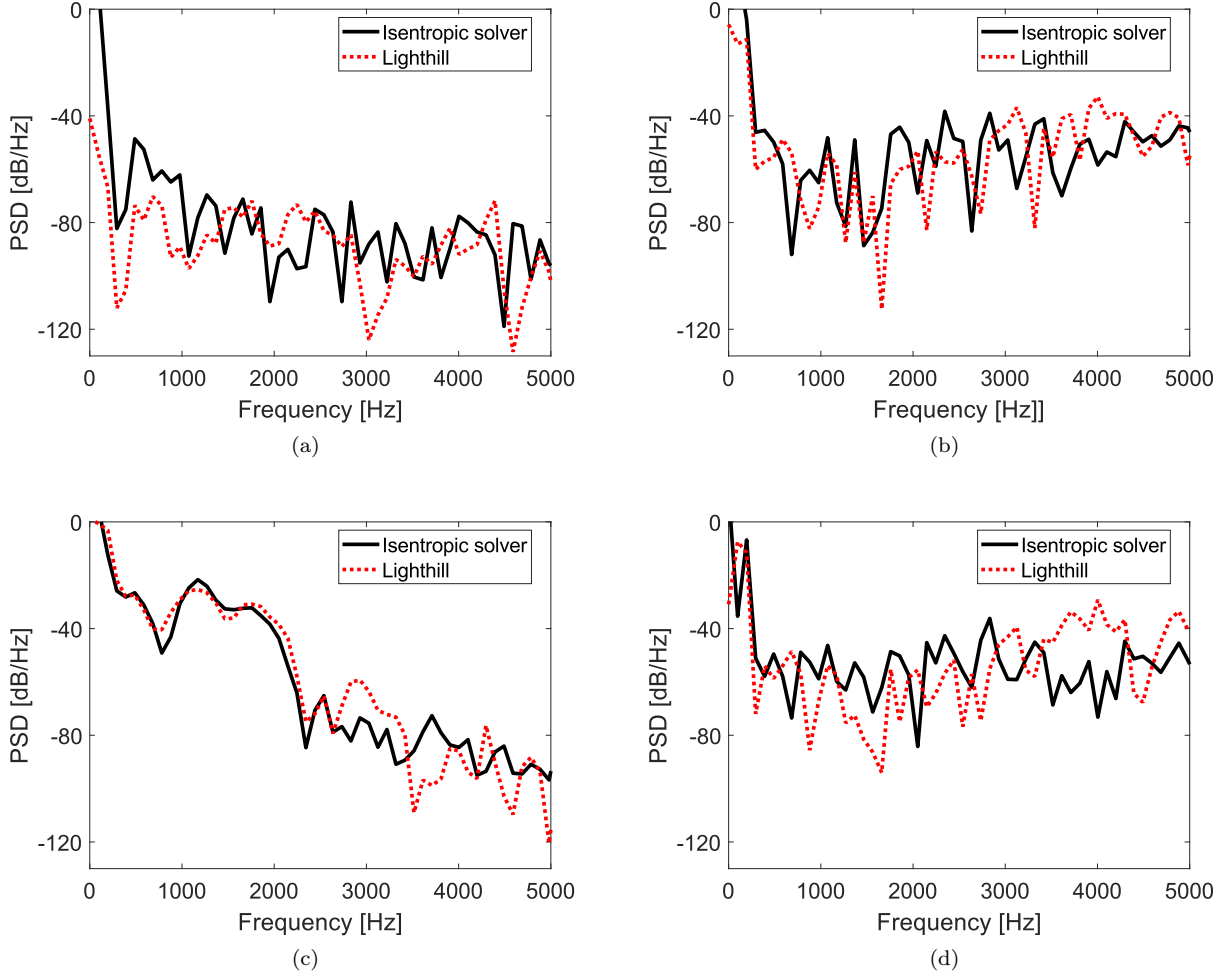
Figure 5: Total acoustic pressure spectrum at the far-field reference points (a) $P1$, (b) $P2$, (c) $P3$ and (d) $P4$ of Fig. 2. Comparison between the hybrid splitting CAA approach (Lighthill) and the isentropic compressible solver.

with respect to the chord line at γ_0). It is also worth mentioning that the non-reflecting conditions for the acoustic fluctuations imposed at the boundary Γ_L (see (28)) work properly as no bouncing waves from Γ_L are detected.

For a more quantitative, rather than qualitative, comparison between the ALE hybrid splitting and isentropic compressible CAA strategies, in Fig. 5 we present the spectra for the total acoustic pressure at the four far-field points $P1 = (-1.4, 0.0)^\top$, $P2 = (0.0, 1.4)^\top$, $P3 = (1.4, 0.0)^\top$ and $P4 = (0.0, -1.4)^\top$ depicted in Fig. 2. As mentioned before, the far-field acoustic field has a dipole pattern, which means that the spectra for points $P2$ and $P4$ in Figs 5b and d should be substantially higher than those of points $P1$ and $P3$ in Figs 5a and c. This is clearly appreciated in the figures, specially for the mid-high frequency range where the levels at $P2$ and $P4$ are ~ 30 dB higher than those of $P1$ and $P3$. On the other hand, the spectra of $P1$ and $P3$ exhibit significant differences. The latter has much larger low frequency content. This is due to the fact that the flow wake, though weakened, is still active at $P3$ and the pressure becomes affected by passing vortices. It is to be noted that Lighthill's analogy is not actually reliable for points like $P3$, which are still in the flow region, as the analogy cannot distinguish sound from pseudo-sound. More elaborated acoustic wave operators should be used instead (see the Introduction section for alternatives). However, the
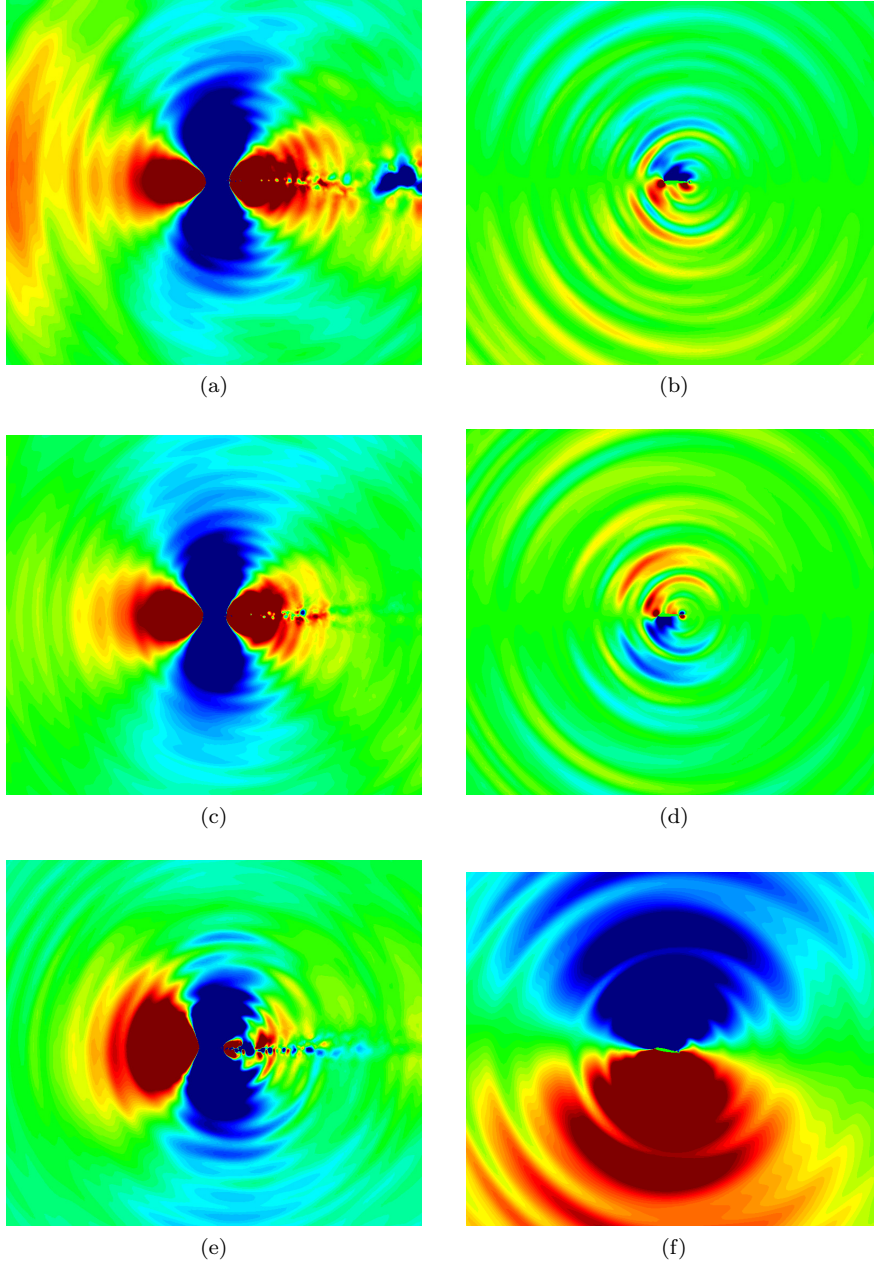
Figure 6: Incident (first column) and diffracted (second column) acoustic pressure for the ALE hybrid CAA Lighthill approach for different angles of attack: $\gamma_0 = 0°$ (first row), $\gamma_{min} = -1.5°$ (second row) and $\gamma_{max} = 10.5°$ (third row).

results for the isentropic compressible solver closely resemble those of Lighthill for $P3$. In fact, despite some peak differences the spectra computed with the two methods at all points exhibit similar average trends.

Fig. 6 shows the incident (first column) and diffracted (second column) acoustic fields obtained from the numerical solution of equations (22) and (23) in the hybrid CAA (Lighthill) approach. As in previous figures, rows from one to three respectively correspond to angles of attack γ_0, γ_{min} and γ_{max}. It is clear from Figs. 6a, c and e that the incident field has a general quadrupole character, while the diffracted one is dominant at the far field and has a dipole pattern, even if the airfoil is moving (see the explanations following
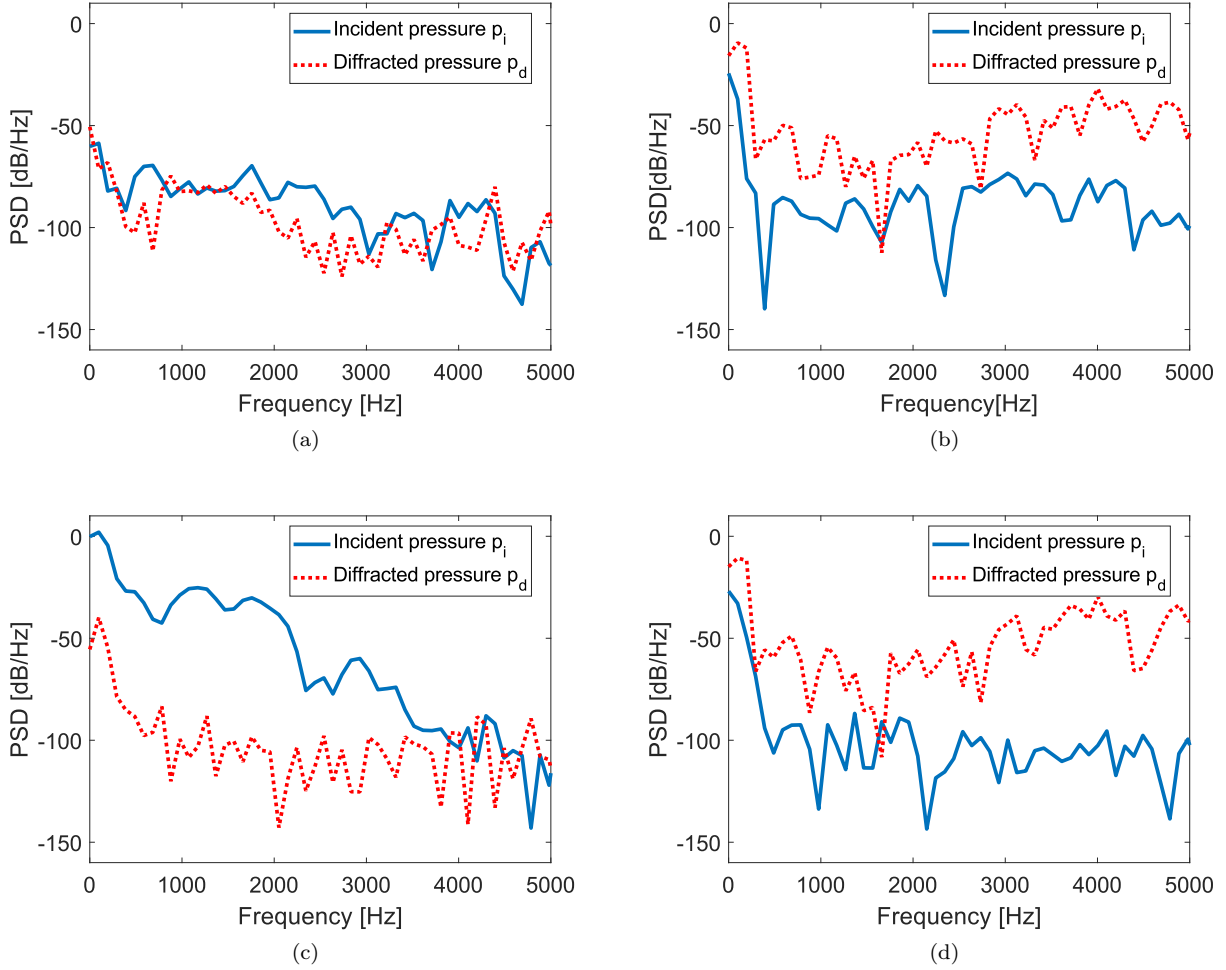
Figure 7: Incident and diffracted acoustic pressure components of the total hybrid CAA spectra in Fig. 5 for points (a) $P1$, (b) $P2$, (c) $P3$ and (d) $P4$ of Fig. 2.

equation (3) in section 2.1.). As expected, the violent and earlier detachment of the boundary layer for $\gamma_{\max}$ in Fig. 6f produces a much stronger dipole than those for γ_0 and $\gamma_{\min}$ in Figs. 6b and d (as also observed for the isentropic compressible solver in Fig. 4f). Finally, in Fig. 7, we have plotted the spectra of the incident and diffracted acoustic pressure components at points $P1$, $P2$, $P3$ and $P4$. The energy summation of these spectra at each point provides the total ones depicted in Fig. 5 for the hybrid CAA strategy. The results confirm previous considerations. As observed, at the far-field points $P2$ and $P4$, which are aligned with the dipole axis, the diffracted noise clearly dominates the spectra for the whole frequency range and almost justifies the total acoustic pressure levels of Figs. 5b and c. The situation is not so clear for points $P1$ and $P3$ in the normal axis of the dipole, as almost no diffracted noise is emitted in that direction. For $P1$ in Fig. (7)a, it can be seen that the incident acoustic pressure field is somewhat larger than the diffracted one for almost all frequencies. For point $P3$ in Fig. (7)c, the dominance of the incident acoustic pressure is very apparent. As explained before, this point is placed in the wake of the airfoil, and despite the long distance apart, weakened vortices still cross it, resulting in the high incident pressure level at low frequencies. As mentioned, such pressure probably cannot be fully associated to acoustic waves.
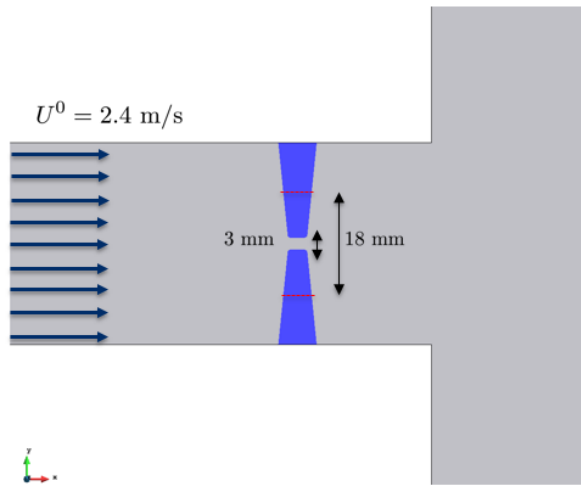
20

Figure 8: Scheme of the computational domain close to the duct exit. The teeth-shaped obstacle evolves from minimum to maximum opening. Only a portion of the outer domain is shown in the figure.
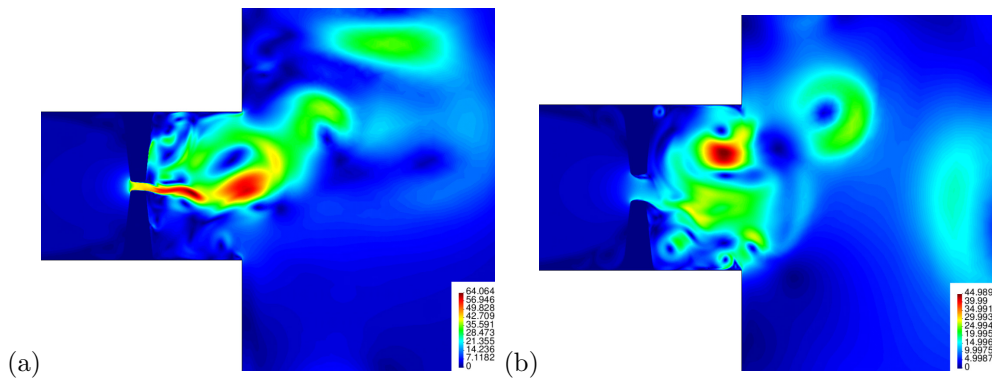

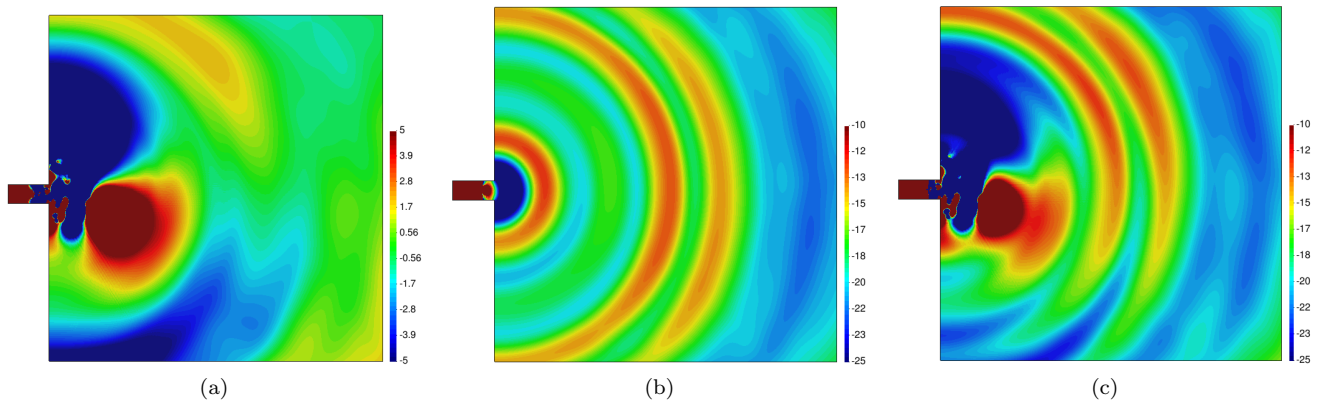Figure 9: Evolution of the flow velocity at (a) $t = 0.02$ (minimum aperture) (b) $t = 0.04$ (maximum aperture).

Figure 10: Incident (a), diffracted (b) and total (c) acoustic pressure in the central section of the domain at $t = 0.02$.
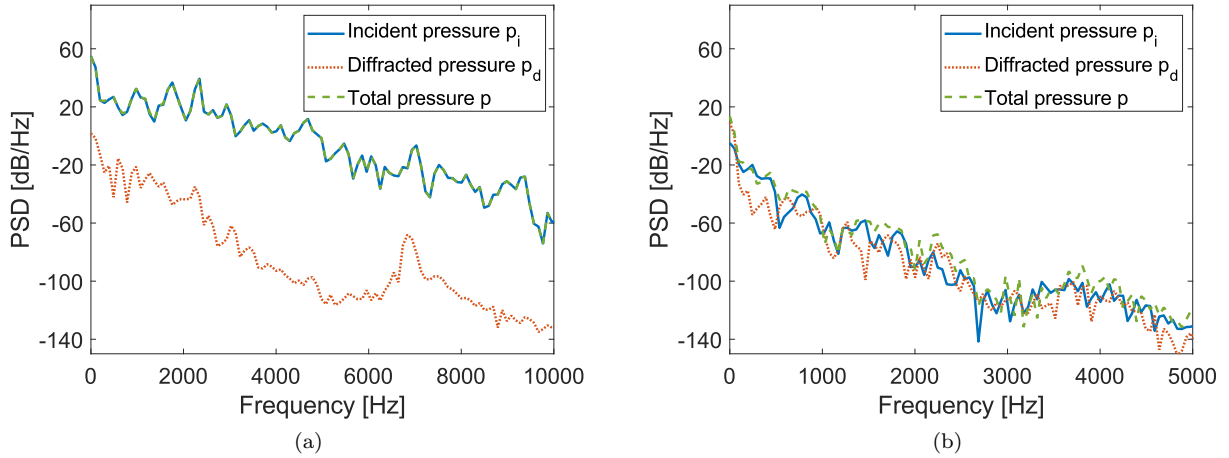
21

Figure 11: Spectra of the incident, diffracted and total acoustic pressure for (a) point $P1$ located at the exit of the duct and (b) point $P2$ located at one corner of the computational domain.

5.2. Aeroacoustics of a two-dimensional opening teeth-shaped obstacle

As a second example, we address the aeroacoustics problem of a flow exiting a duct whose termination slowly transitions from an initial small aperture to a larger one. This type of situations is important, for instance, in numerical voice generation. A sibilant sound like /s/ is produced when the flow emanating from the lungs is accelerated by moving the tongue upwards to the hard palate, which results in a small air constriction. The turbulent air jet that goes through it impinges on the upper teeth and then passes through the inter-dental space generating strong vortices between the lower teeth and lower lips, which in turn trigger acoustic waves. The latter propagate outwards and also become diffracted by the teeth [1, 2, 4, 68]. The vocal tract geometry in the generation of a single sibilant is basically static, but if one attempts to generate more complex sounds like sibilant-vowel syllables (e.g., /sa/) the vocal tract will change its shape and the inter-dental aperture will vary [3, 69]. The current example may be viewed as a very simplified model related to some of the physics underlying such voice generation problem. Only the hybrid splitting CAA approach will be applied in this section as comparisons with the isentropic solver have been already performed in the previous one, and separating the contributions from the direct and diffracted acoustic waves is what usually matters to better understand sibilant generation processes (see e.g., [2, 68]).

The problem at hand consists of a three-dimensional computational domain in which a duct exits at a flat baffle. The spanwise dimension is though very small so the acoustic results are essentially two-dimensional. A sketch illustrating the central section of the geometry is depicted in Fig. 8. The duct has a length of 0.09 and a teeth-shaped termination which transitions from an initial aperture of 3×10^{-3} to a final one of 18×10^{-3}, according to a prescribed velocity ramp. Since the analysis focuses on the contribution of the direct and diffracted acoustic pressure contributions of the termination, the opening starts at $t = 0.02$, once the flow and acoustic field have fully developed, and finishes at $t = 0.04$. The inlet velocity is 2.4 and a time step of $\Delta t = 10^{-5}$ has been used for the simulations. The exit domain has dimensions $1 \times 1 \times 0.025$. As in the previous example, equal interpolation has been used for the acoustic pressure and acoustic particle velocity and an unstructured mesh of $\sim 3.4 \times 10^5$ elements has been employed to discretize the computational domain.

The initial occlusion induces an air jet whose oscillations shed aperiodic vortices of various dimensions, which produce acoustic waves covering a wide range of frequencies and a high noise level. The jet clearly manifests in the snpahshot for the incompressible velocity field at $t = 0.02$, in Fig. 9a. Once the termination is totally opened at $t = 0.04$, the jet has lost most of its power and larger and slower vortices are shed from the duct termination, see Fig. 9b. On the other hand, in Fig. 10 we have plotted snapshots for the

<div align="center">22</div>

incident, diffracted and total acoustic pressure at $t = 0.02$. As observed, and as one could expect, the total acoustic pressure in Fig. 10c is a combination of the incident one in Fig. 10a and the diffracted pressure in Fig. 10b (note that the colour scales change from one figure to another to better appreciate their contents). The incident pressure mainly dominates the near field total pressure while the diffracted field is mostly responsible for the total acoustic pressure at the far field. However, at the far field the incident pressure still manifests as vortices are shed in several directions from the duct exit (see Fig. 9), resulting in a disorganized wake affecting the whole computational domain. This can be clearly appreciated if we plot the spectra of the incident and diffracted waves and the total spectra for two points respectively placed close to the duct exit and far away from it. Let us consider $P1 = (0.09, 0.025, -0, 0125)$ at the exit of the duct and $P2 = (0.98, 0.47, -0.0125)$ at one corner of the computational domain (whose origin is centered at the entrance of the duct). While the spectra of $P1$ is totally determined by the incident field the diffracted one being negligible (see Fig 11a), in the case of $P2$, both, the incident and diffracted acoustic fields equally contribute to the total acoustic pressure (see Fig 11b). As said before, the fact that the incident pressure is still of importance at $P2$ is because shed vortices are still active in the region. If the minimum aperture of the teeth-shaped termination was kept constant, the vortex wake would be more focused and would have less influence on $P2$. In such circumstance the diffracted field would be dominant at that point, similarly to what happened for $P2$ and $P4$ in the case of the NACA airfoil.

6. Conclusions

In this work, we have expanded some previous research on CAA at low Mach numbers to the case of flow sound generated in the presence of slowly moving bodies. In particular, the hybrid CAA approach in [6], which was able to separate the incident and diffracted noise contributions of rigid objects to far-field points, has been adapted to account for the slow motion of such objects. In such circumstances, the thickness noise turns to be negligible and the loading noise aeroacoustics can be posed as a quasi-static diffraction problem. The latter is numerically solved with FEM and by setting the involved equations in an ALE framework. The incompressible ALE Navier-Stokes equations are first resolved to obtain the acoustic source term and then the acoustic pressure field is determined. It is to be mentioned that it is not possible to set the irreducible acoustic wave equation in an ALE framework and one has to deal with its mixed formulation, which requires FEM stabilization strategies, as presented. For comparison, we have also introduced an ALE version of the direct CAA strategy in [7], consisting of an isentropic compressible solver.

The proposed formulations have been tested in two situations. The first one consists of a 2D oscillating NACA0012 airfoil. The hybrid ALE CAA method and the isentropic compressible ALE solver have provided similar results for the total acoustic pressure. Furthermore, the simulations of the former clearly show the quadrupole character of the incident noise field and the dipole pattern of the diffracted field. As expected, when the airfoil motion reaches its higher angle of attack the aerodynamic noise strongly increases because the boundary layer detaches close to the leading edge and sheds large vortices. For far-field points at right angle to the static airfoil chord, the diffracted noise is totally responsible for the total noise, while for points located in the axis of the chord in front of the airfoil, the incident noise dominates. For points in the wake both the incident and diffracted fields have similar contributions. On the other hand, the second example has consisted in a duct with a teeth-shaped termination that progressively opens from a small aperture to a large one. Such case reminds of situations found in the numerical production of voice, like in the generation of a syllable involving a sibilant sound like /s/, which is of an aeroacoustic nature. The obtained results indicate that in the near field the contribution of the incident acoustic pressure dominates. At the far field, the diffraction component would be the most important one for small teeth apertures, but for large apertures vortices are shed in many directions balancing the contributions of the incident and diffracted components to the total acoustic pressure. It is expected that the proposed numerical strategies could be particularly helpful for future developments in numerical voice production.

References

[1] T. Yoshinaga, K. Nozaki, S. Wada, Experimental and numerical investigation of the sound generation mechanisms of sibilant fricatives using a simplified vocal tract model, Phys. Fluids 30 (2018) 035104.

[2] A. Pont, O. Guasch, J. Baiges, R. Codina, A. Van Hirtum, Computational aeroacoustics to identify sound sources in the generation of sibilant/s/, Int. J. Numer. Meth. Biomed. Engrg. 35 (2019) e3153.

[3] T. Yoshinaga, K. Nozaki, A. Iida, Hysteresis of aeroacoustic sound generation in the articulation of [s], Phys. Fluids 32 (2020) 105114.

[4] A. Pont, O. Guasch, M. Arnela, Finite element generation of sibilants/s/and/z/using random distributions of Kirchhoff vortices, Int. J. Numer. Meth. Biomed. Engrg. 36 (2020) e3302.

[5] W. Xu, Q. Wang, D. Wu, Q. Li, Simulation and design improvement of a low noise control valve in autonomous underwater vehicles, Appl. Acoust. 146 (2019) 23–30.

[6] O. Guasch, A. Pont, J. Baiges, R. Codina, Concurrent finite element simulation of quadrupolar and dipolar flow noise in low Mach number aeroacoustics, Comput. Fluids 133 (2016) 129–139.

[7] A. Pont, R. Codina, J. Baiges, O. Guasch, Unified solver for fluid dynamics and aeroacoustics in isentropic gas flows, J. Comput. Phys. 363 (2018) 11–29.

[8] M. J. Lighthill, On sound generated aerodynamically. I. general theory, Proc. R. Soc. Lond. A 211 (1952) 564–587.

[9] C. Bailly, C. Bogey, X. Gloerfelt, Some useful hybrid approaches for predicting aerodynamic noise, C. R. Mec. 333 (2005) 666–675.

[10] H. S. Ribner, Aerodynamic sound from fluid dilitations; a theory of the sound from jets and other flows, UTIA Report, No. 86, AFOSR TN 3430 (1962).

[11] M. Roger, The acoustic analogy some theoretical background, Lecture series-van Kareman Institute for fluid dynamics 2 (2000) A1–A32.

[12] O. M. Phillips, On the generation of sound by supersonic turbulent shear layers, J. Fluid Mech. 9 (1960) 1–28.

[13] G. Lilley, On the noise from jets: AGARD CP-131, Technical Report, IS. 1.: sn, 1974.

[14] A. Powell, Theory of vortex sound, J. Acoust. Soc. Am. 36 (1964) 177–195.

[15] M. Howe, The generation of sound by aerodynamic sources in an inhomogeneous steady flow, J. Fluid Mech. 67 (1975) 597–610.

[16] W. Möhring, On vortex sound at low Mach number, J. Fluid Mech. 85 (1978) 685–691.

[17] M. Goldstein, A generalized acoustic analogy, J. Fluid Mech. 488 (2003) 315–333.

[18] N. Curle, The influence of solid boundaries upon aerodynamic sound, Proc. R. Soc. Lond. A 231 (1955) 505–514.

[19] J. F. Williams, D. L. Hawkings, Sound generation by turbulence and surfaces in arbitrary motion, Phil. Trans. Roy. Soc. A 264 (1969) 321–342.

[20] C. Bailly, D. Juve, Numerical solution of acoustic propagation problems using linearized Euler equations, AIAA J. 38 (2000) 22–29.

[21] C. Bailly, C. Bogey, Contributions of computational aeroacoustics to jet noise research and prediction, Int. J. Comput. Fluid Dyn. 18 (2004) 481–491.

[22] G. Djambazov, C.-H. Lai, K. Pericleous, On the coupling of Navier–Stokes and linearised Euler equations for aeroacoustic simulation, Comput. Visual. Sci. 3 (2000) 9–12.

[23] X. Gloerfelt, C. Bogey, C. Bailly, Numerical evidence of mode switching in the flow-induced oscillations by a cavity, Int. J. Aeroacoust. 2 (2003) 193–217.

[24] R. Ewert, W. Schröder, Acoustic perturbation equations based on flow decomposition via source filtering, J. Comput. Phys. 188 (2003) 365–398.

[25] A. Hueppe, M. Kaltenbacher, Spectral finite elements for computational aeroacoustics using acoustic perturbation equations, J. Comput. Acoust. 20 (2012) 1240005.

[26] O. Guasch, P. Sánchez-Martín, A. Pont, J. Baiges, R. Codina, Residual-based stabilization of the finite element approximation to the acoustic perturbation equations for low Mach number aeroacoustics, Int. J. Numer. Meth. Fluids 82 (12) (2016) 839–857.

[27] S. Schoder, M. Kaltenbacher, Hybrid aeroacoustic computations: State of art and new achievements, J. Theor. Comput. Acoust. 27 (2019) 1950020.

[28] P. Martínez-Lera, C. Schram, H. Bériot, R. Hallez, An approach to aerodynamic sound prediction based on incompressible-flow pressure, J. Sound Vib. 333 (2014) 132–143.

[29] A. A. Oberai, F. Roknaldin, T. J. R. Hughes, Computation of trailing-edge noise due to turbulent flow over an airfoil, AIAA J. 40 (2002) 2206–2216.

[30] O. Guasch, R. Codina, An algebraic subgrid scale finite element method for the convected Helmholtz equation in two dimensions with applications in aeroacoustics, Comput. Methods Appl. Mech. Engrg. 196(45–48) (2007) 4672–4689.

[31] O. Guasch, R. Codina, Computational aeroacoustics of viscous low speed flows using subgrid scale finite element methods, J. Comput. Acoust. 17(3) (2009) 309–330.

[32] M. Kaltenbacher, M. Escobar, S. Becker, I. Ali, Numerical simulation of flow-induced noise using LES/SAS and lighthill's acoustic analogy, Int. J. Numer. Meth. Fluids 63 (2010) 1103–1122.

[33] P. Doak, Acoustic radiation from a turbulent fluid containing foreign bodies, Proc. R. Soc. Lond. A 254 (1960) 129–146.

[34] D. Crighton, Basic principles of aerodynamic noise generation, Prog. Aerosp. Sci. 16 (1975) 31–96.

[35] X. Gloerfelt, F. Pérot, C. Bailly, D. Juvé, Flow-induced cylinder noise formulated as a diffraction problem for low Mach numbers, J. Sound Vib. 287 (2005) 129–151.

[36] T. Hughes, W. Liu, T. Zimmermann, Lagrangian-Eulerian finite-element formulation for compressible viscous flows, Comput. Methods Appl. Mech. Engrg. 29 (1981) 329–349.

[37] A. Huerta, W. Liu, Viscous flow with large free surface motion, Comput. Methods Appl. Mech. Engrg. 69 (1988) 277–324.

[38] O. Guasch, M. Arnela, R. Codina, H. Espinoza, A stabilized finite element method for the mixed wave equation in an ALE framework with application to diphthong production, Acta Acust. united Ac. 102 (2016) 94–106.

[39] R. Codina, Finite element approximation of the hyperbolic wave equation in mixed form, Comput. Methods Appl. Mech. Engrg. 197(13–16) (2008) 1305–1322.

[40] S. Parada, J. Baiges, R. Codina, A fractional step method for computational aeroacoustics using weak imposition of Dirichlet boundary conditions, Comput. Fluids 197 (2020) 104374.

[41] D. Crighton, A. Dowling, J. Ffowcs Williams, M. Heckl, F. Leppington, Modern Methods in Analytical Acoustics-Lecture Notes, Springer-Verlag (1992).

[42] J. Wong, D. Darmofal, J. Peraire, The solution of the compressible Euler equations at low Mach numbers using a stabilized finite element algorithm, Comput. Methods Appl. Mech. Engrg. 190 (2001) 5719–5737.

[43] T. Colonius, S. K. Lele, P. Moin, Boundary conditions for direct computation of aerodynamic sound generation, AIAA J. 31 (1993) 1574–1582.

[44] T. Colonius, Modeling artificial boundary conditions for compressible flow, Annu. Rev. Fluid Mech. 36 (2004) 315–345.

[45] T. Yabe, P.-Y. Wang, Unified numerical procedure for compressible and incompressible fluid, J. Phys. Soc. Japan 60 (1991) 2105–2108.

[46] F. Xiao, R. Akoh, S. Ii, Unified formulation for compressible and incompressible flows by using multi-integrated moments ii: Multi-dimensional version for compressible and incompressible flows, J. Comput. Phys. 213 (2006) 31–56.

[47] L. Pesch, J. J. van der Vegt, A discontinuous Galerkin finite element discretization of the Euler equations for compressible and incompressible fluids, J. Comput. Phys. 227 (2008) 5426–5446.

[48] C. Bayona, J. Baiges, R. Codina, Solution of low Mach number aeroacoustic flows using a Variational Multi-Scale finite element formulation of the compressible Navier–Stokes equations written in primitive variables, Comput. Methods Appl. Mech. Engrg. 344 (2019) 1073–1103.

[49] M. Billaud, G. Gallice, B. Nkonga, A simple stabilized finite element method for solving two phase compressible–incompressible interface flows, Comput. Methods Appl. Mech. Engrg. 200 (2011) 1272–1290.

[50] M. Juntunen, R. Stenberg, Nitsche's method for general boundary conditions, Mathematics of computation 78 (2009) 1353–1374.

[51] J. Berenger, A perfectly matched layer for the absorption of electromagnetic waves, J. Comput. Phys. 114 (2) (1994) 185–200.

[52] F. Q. Hu, Development of PML absorbing boundary conditions for computational aeroacoustics: A progress review, Comput. Fluids 37 (2008) 336–348.

[53] T. Hughes, Multiscale phenomena: Green's function, the Dirichlet-to-Neumann formulation, subgrid scale models, bubbles and the origins of stabilized formulations, Comput. Methods Appl. Mech. Engrg. 127 (1995) 387–401.

[54] T. J. Hughes, G. R. Feijóo, L. Mazzei, J.-B. Quincy, The variational multiscale methodâ ĂTa paradigm for computational mechanics, Computer methods in applied mechanics and engineering 166 (1998) 3–24.

[55] R. Codina, Stabilized finite element approximation of transient incompressible flows using orthogonal subscales, Comput. Methods Appl. Mech. Engrg. 191 (2002) 4295–4321.

[56] R. Codina, J. Principe, O. Guasch, S. Badia, Time dependent subscsales in the stabilized finite element approximation of incompressible flow problems, Comput. Methods Appl. Mech. Engrg. 196(21–24) (2007) 2413–2430.

[57] O. Guasch, R. Codina, Statistical behavior of the orthogonal subgrid scale stabilization terms in the finite element large eddy simulation of turbulent flows, Comput. Methods Appl. Mech. Engrg. 261 (2013) 154–166.

[58] O. Colomés, S. Badia, R. Codina, J. Principe, Assessment of variational multiscale models for the large eddy simulation of turbulent incompressible flows, Comput. Methods Appl. Mech. Engrg. 285 (2015) 32–63.

[59] O. Guasch, A. Pont, J. Baiges, R. Codina, Simultaneous finite element computation of direct and diffracted flow noise in domains with static and moving walls, in: International Conference on Flow Induced Noise and Vibration Issues and Aspects (2017), Springer, pp. 179–194.

[60] M. S. Howe, Acoustics of fluid-structure interactions, Cambridge university press, 1998.

[61] H. Espinoza, R. Codina, S. Badia, A Sommerfeld non-reflecting boundary condition for the wave equation in mixed form, Comput. Methods Appl. Mech. Engrg. 276 (2014) 122–148.

[62] R. Codina, J. González-Ondina, G. Díaz-Hernández, J. Principe, Finite element approximation of the modified Boussinesq equations using a stabilized formulation, Int. J. Numer. Meth. Fluids 57(9) (2008) 1249–1268.

[63] C. Bayona, J. Baiges, R. Codina, Variational multi-scale finite element approximation of the compressible Navier-Stokes equations, Int J. Numer. Meth. Heat Fluid Flow (2016).

[64] R. Codina, J. Baiges, Approximate imposition of boundary conditions in immersed boundary methods, International Journal for Numerical Methods in Engineering 80 (2009) 1379–1405.

[65] R. Codina, On stabilized finite element methods for linear systems of convection–diffusion-reaction equations, Comput. Methods Appl. Mech. Engrg. 188 (2000) 61–82.

[66] G. Chiandussi, G. Bugeda, E. Oñate, A simple method for automatic update of finite element meshes, Int. J. Numer. Meth. Biomed. Engrg. 16 (2000) 1–19.

[67] W. R. Wolf, S. K. Lele, Trailing edge noise predictions using compressible les and acoustic analogy, in: Proceedings of the 17th AIAA/CEAS Aeroacoustics Conference, AIAA Paper, volume 2784, pp. 1–25.

[68] M. Howe, R. McGowan, Aeroacoustics of [s], Proc. R. Soc. A 461 (2005) 1005–1028.

[69] M. Arnela, O. Guasch, Finite element simulation of/asa/in a three-dimensional vocal tract using a simplified aeroacoustic source model, Universitätsbibliothek der RWTH Aachen, 2019.